

CHINA CDC WEEKLY



Vol. 7 No. 14 Apr. 4, 2025

中国疾病预防控制中心周报

 World Health Day April 7, 2025 <i>Healthy beginnings, hopeful futures</i>	Perspectives	
	World Health Day 2025: Time to Change Mindset Beyond Global Commitment to Maternal Health and Women's Well-Being	449
	Vital Surveillances	
	Changing Patterns of Epidemiological Characteristics and Spatial-Temporal Clusters of Human Brucellosis Based on County Level — China, 2011–2023	453
	Epidemiological Evolution Profile of Human Brucellosis and Socioeconomic Factor Correlation Analysis — Southern and Northern Areas, China, 1950–2021	460
	Preplanned Studies	
	Epidemic Characteristics of Schistosomiasis — China, 2016–2023	467
Methods and Applications		
A Novel Matching Pursuit Modeling Strategy Based on Adaptive Fourier Decomposition Theory for Predicting Antigenic Variation of Influenza A (H1N1)	473	
Development of A Novel EvaGreen-Dye Based Recombinase Aided Amplification Assay Using Self-Avoiding Molecular Recognition System Primers	482	
Notifiable Infectious Diseases Reports		
Reported Cases and Deaths of National Notifiable Infectious Diseases — China, February 2025	489	



ISSN 2096-7071



Editorial Board

Editor-in-Chief Hongbing Shen

Founding Editor George F. Gao

Deputy Editor-in-Chief Liming Li Gabriel M Leung Zijian Feng

Executive Editor Chihong Zhao

Members of the Editorial Board

Rui Chen	Wen Chen	Xi Chen (USA)	Zhuo Chen (USA)
Gangqiang Ding	Xiaoping Dong	Pei Gao	Mengjie Han
Yuantaao Hao	Na He	Yuping He	Guoqing Hu
Zhibin Hu	Yueqin Huang	Na Jia	Weihua Jia
Zhongwei Jia	Guangfu Jin	Xi Jin	Biao Kan
Haidong Kan	Ni Li	Qun Li	Ying Li
Zhenjun Li	Min Liu	Qiyong Liu	Xiangfeng Lu
Jun Lyu	Huilai Ma	Jiaqi Ma	Chen Mao
Xiaoping Miao	Ron Moolenaar (USA)	Daxin Ni	An Pan
Lance Rodewald (USA)	William W. Schluter (USA)	Yiming Shao	Xiaoming Shi
Yuelong Shu	RJ Simonds (USA)	Xuemei Su	Chengye Sun
Quanfu Sun	Xin Sun	Feng Tan	Jinling Tang
Huaqing Wang	Hui Wang	Linhong Wang	Tong Wang
Guizhen Wu	Jing Wu	Xifeng Wu (USA)	Yongning Wu
Min Xia	Ningshao Xia	Yankai Xia	Lin Xiao
Hongyan Yao	Zundong Yin	Dianke Yu	Hongjie Yu
Shicheng Yu	Ben Zhang	Jun Zhang	Liubo Zhang
Wenhua Zhao	Yanlin Zhao	Xiaoying Zheng	Maigeng Zhou
Xiaonong Zhou	Guihua Zhuang		

Advisory Board

Director of the Advisory Board Jiang Lu

Vice-Director of the Advisory Board Yu Wang Jianjun Liu Jun Yan

Members of the Advisory Board

Chen Fu	Gauden Galea (Malta)	Dongfeng Gu	Qing Gu
Yan Guo	Ailan Li	Jiafa Liu	Peilong Liu
Yuanli Liu	Kai Lu	Roberta Ness (USA)	Guang Ning
Minghui Ren	Chen Wang	Hua Wang	Kean Wang
Xiaoqi Wang	Zijun Wang	Fan Wu	Xianping Wu
Jingjing Xi	Jianguo Xu	Gonghuan Yang	Tilahun Yilma (USA)
Guang Zeng	Xiaopeng Zeng	Yonghui Zhang	Bin Zou

Editorial Office

Directing Editor Chihong Zhao

Managing Editors Yu Chen

Senior Scientific Editors Daxin Ni Ning Wang Wenwu Yin Jianzhong Zhang Qian Zhu

Scientific Editors

Weihong Chen	Tao Jiang	Xudong Li	Nankun Liu	Liwei Shi	Liuying Tang
Meng Wang	Zhihui Wang	Qi Yang	Qing Yue	Lijie Zhang	Ying Zhang

Perspectives

World Health Day 2025: Time to Change Mindset Beyond Global Commitment to Maternal Health and Women's Well-Being

Minmin Wang^{1,2}; Minghui Ren^{1,2,3,4,#}

ABSTRACT

The World Health Day 2025 calls for a global commitment to maternal health. Maternal health has long been a central focus in the global health agenda, prominently featured in both the Millennium Development Goals and Sustainable Development Goals. Substantial progress has been made in reducing maternal mortality through international collaboration. However, significant challenges persist, including reductions in global health financing and emerging threats such as climate change. Mindset changes are urgently needed for maternal health and broader global health governance. Sustainable investment and health system strengthening are imperative. Global health governance should be reformed through a paradigm shift toward an accountable, fair, efficient, and transparent ecosystem.

World Health Day 2025, to be celebrated on April 7, will launch “Healthy Beginnings, Hopeful Futures”, a year-long global campaign focused on advancing maternal and newborn health (1). This initiative emphasizes the critical need to eliminate preventable maternal and newborn deaths and calls for enhanced collaboration across governments, international organizations, and the global health community.

Each year, approximately 210 million women become pregnant, underscoring that maternal health is not a peripheral issue, but a central global health priority (2). Pregnancy, while a life-altering event, introduces elevated biological and social vulnerabilities, particularly for women in resource-limited settings. Obstetric complications, including hemorrhage, hypertensive disorders, and infections, remain the predominant causes of maternal mortality (3–4). Additionally, maternal mental health has emerged as a critical dimension requiring urgent attention (5). Maternal health also has profound intergenerational

implications. Undernutrition during pregnancy constitutes a major determinant of both childhood stunting and the subsequent development of obesity and non-communicable diseases in adulthood (6–8). Thus, maternal health is intrinsically linked not only to women's wellbeing but to the broader health trajectory of societies, particularly within the framework of sustainable development.

Progress and Milestones in Maternal Health

Maternal health has been a cornerstone of the global health agenda for decades, with significant milestones dating back to the 1976–1985 period (9). The United Nations (UN) Decade for Women, the Alma-Ata Declaration on Primary Health Care, and the Convention on the Elimination of All Forms of Discrimination Against Women collectively established the foundational framework for addressing maternal health as a global priority. Subsequently, maternal health was integrated as a central component of the UN's Millennium Development Goals (MDGs), which explicitly aimed to “reduce by three quarters, between 1990 and 2015, the maternal mortality ratio.” (10) In the transition to the Sustainable Development Goals (SDGs), maternal mortality was elevated to the first target under SDG 3, “Good Health and Well-being,” with the ambitious goal of reducing the global maternal mortality ratio to fewer than 70 deaths per 100,000 live births by 2030.

Financial investment has directly reflected the global commitment to maternal health. Development assistance for health (DAH) targeting reproductive and maternal health increased substantially from \$2 billion in 1990 to \$6.32 billion in 2013, stabilizing at \$6.46 billion by 2023. These resources have supported critical initiatives in family planning, maternal health, and health systems strengthening. Private philanthropic contributions have emerged as particularly significant, totaling 1.87 billion US dollars (USD) and constituting the largest funding source in

this domain. The United States remains the predominant governmental donor, contributing 1.85 billion USD, followed by multilateral contributions from other Organization for Economic Cooperation and Development (OECD) countries.

Substantial progress has been achieved in reducing maternal mortality through coordinated international collaboration. Between 1990 and 2015, maternal mortality decreased markedly from an estimated 390,185 deaths in 1990 to 275,288 in 2015 (11–12). This significant reduction was facilitated by comprehensive improvements in health systems, expanded access to essential care, and implementation of robust maternal health policies. From 2000 to 2020, the global maternal mortality ratio (MMR) declined by approximately 34%, from 342 deaths per 100,000 live births to 223 deaths per 100,000 live births (13). The absolute number of global annual maternal deaths also decreased substantially throughout this period, from 447,000 to 287,000, representing a reduction of more than one-third. Globally, the lifetime risk of a 15-year-old girl eventually dying from a maternal cause was nearly halved, declining from 1 in 120 in 2000 to 1 in 210 in 2020 (14).

Challenges Persist in Global Maternal Health

Despite this progress, significant challenges regarding health equity persist. In 2020, approximately 287,000 women died from pregnancy-related causes, with 95% of these deaths occurring in low- and middle-income countries (15). Sub-Saharan Africa and Southern Asia together accounted for 87% (253,000) of global maternal deaths in 2020 (14), highlighting the profound regional disparities that continue to impede progress. From 2000 to 2020, eight countries and territories experienced significant percentage increases in MMR, including the Bolivarian Republic of Venezuela, Cyprus, Greece, the United States, Mauritius, Puerto Rico, Belize, and the Dominican Republic (14). These trends underscore the urgent need for high-quality health services, particularly in crisis settings, unstable situations, and among vulnerable populations.

A reduction in funding and leadership for global maternal health programs threatens to reverse decades of progress, particularly in low- and middle-income countries. The COVID-19 pandemic prompted a substantial reallocation of health funding away from established priorities like maternal and child health

(16). Geopolitical tensions and societal divisions have further undermined the financial sustainability of maternal health programs. Many OECD countries have increasingly redirected financial resources toward geopolitical concerns, such as the ongoing crisis in Ukraine, diverting both attention and critical funding from essential maternal health interventions (17).

Emerging threats also challenge traditional vertical intervention programs. Climate change, with its far-reaching effects on environmental health, escalating heat exposure, food security, and migration, contributes to systemic instability and health system fragility, disproportionately affecting vulnerable populations — especially women and children (18–21). Pregnant women in resource-limited settings are particularly susceptible to climate-related disasters that disrupt healthcare systems and limit access to essential maternal care. Similarly, emerging infectious diseases and the potential for future pandemics pose additional strains on already fragile health systems. These global threats could potentially reverse decades of progress in maternal health without urgent coordinated action.

Mindset Changes Needed for Maternal Health and Broader Global Health Governance

To achieve the SDG target on maternal mortality and enhance women's long-term health and well-being, sustainable investment and health system strengthening are imperative. The majority of maternal deaths are preventable with access to high-quality healthcare. Health system strengthening, particularly at the primary healthcare level, must address the diverse spectrum of maternal and newborn health challenges, including obstetric complications, mental health disorders, noncommunicable diseases, and family planning needs. Integrating maternal health into broader health policies and social development frameworks is essential (22–23). Innovations in healthcare delivery — such as task-shifting to mid-level providers, digital health technologies, and community-based interventions — have demonstrated effectiveness in expanding care access, especially in underserved regions. Furthermore, addressing the intersection of maternal health with climate change and pandemic preparedness requires a holistic approach that prioritizes health system resilience and sustainability (24).

The current geopolitical landscape has exposed the

vulnerability of traditional vertical intervention programs that rely heavily on external development assistance for health. The time has come to change the mindset for global maternal health and women's well-being. Global health governance must be reformed into an accountable, fair, efficient, and transparent ecosystem. At its foundation, health should be established as a fundamental priority across all nations. A strengthened primary healthcare system should serve as the foundation for supporting healthy pregnancies, enhancing postnatal care, and advancing the broader objective of creating a healthier world.

On World Health Day 2025, global partners should reaffirm their commitment to reducing maternal mortality and improving women's long-term health and well-being by increasing both financial contributions and technical support. Simultaneously, developing countries must enhance domestic health investments to collaboratively build resilient health systems at national, regional, and global levels.

Conflicts of interest: No conflicts of interest.

doi: 10.46234/ccdcw2025.074

* Corresponding author: Minghui Ren, renminghui@pku.edu.cn.

¹ Department of Global Health, School of Public Health, Peking University, Beijing, China; ² Beijing Institute for Health Development, Peking University, Beijing, China; ³ Institute for Global Health, Peking University, Beijing, China; ⁴ China Center for Health Development Studies, Peking University, Beijing, China.

Copyright © 2025 by Chinese Center for Disease Control and Prevention. All content is distributed under a Creative Commons Attribution Non Commercial License 4.0 (CC BY-NC).

Submitted: February 26, 2025

Accepted: March 23, 2025

Issued: April 04, 2025

REFERENCES

- World Health Organization. World health day 2025: healthy beginnings, hopeful futures. 2025. <https://www.who.int/news-room/events/detail/2025/04/07/default-calendar/world-health-day-2025-healthy-beginnings-hopeful-futures>. [2025-2-20].
- Graham W, Woodd S, Byass P, Filippi V, Gon G, Virgo S, et al. Diversity and divergence: the dynamic burden of poor maternal health. *Lancet* 2016;388(10056):2164 – 75. [https://doi.org/10.1016/S0140-6736\(16\)31533-1](https://doi.org/10.1016/S0140-6736(16)31533-1).
- Khan KS, Wojdyla D, Say L, Gülmezoglu AM, Van Look PF. WHO analysis of causes of maternal death: a systematic review. *Lancet* 2006;367(9516):1066 – 74. [https://doi.org/10.1016/S0140-6736\(06\)68397-9](https://doi.org/10.1016/S0140-6736(06)68397-9).
- Say L, Chou D, Gemmill A, Tunçalp Ö, Moller AB, Daniels J, et al. Global causes of maternal death: a WHO systematic analysis. *Lancet Glob Health* 2014;2(6):e323 – 33. [https://doi.org/10.1016/S2214-109X\(14\)70227-X](https://doi.org/10.1016/S2214-109X(14)70227-X).
- Howard LM, Piot P, Stein A. No health without perinatal mental health. *Lancet* 2014;384(9956):1723 – 4. [https://doi.org/10.1016/S0140-6736\(14\)62040-7](https://doi.org/10.1016/S0140-6736(14)62040-7).
- Wells JCK. The capacity-load model of non-communicable disease risk: understanding the effects of child malnutrition, ethnicity and the social determinants of health. *Eur J Clin Nutr* 2018;72(5):688 – 97. <https://doi.org/10.1038/s41430-018-0142-x>.
- Wells JC, Sawaya AL, Wibaek R, Mwangome M, Poullas MS, Yajnik CS, et al. The double burden of malnutrition: aetiological pathways and consequences for health. *Lancet* 2020;395(10217):75 – 88. [https://doi.org/10.1016/S0140-6736\(19\)32472-9](https://doi.org/10.1016/S0140-6736(19)32472-9).
- Grey K, Gonzales GB, Abera M, Lelijveld N, Thompson D, Berhane M, et al. Severe malnutrition or famine exposure in childhood and cardiometabolic non-communicable disease later in life: a systematic review. *BMJ Glob Health* 2021;6(3):e003161. <https://doi.org/10.1136/bmjgh-2020-003161>.
- Smith SL, Rodriguez MA. Agenda setting for maternal survival: the power of global health networks and norms. *Health Policy Plan* 2016;31(suppl_1):i48 – 59. <https://doi.org/10.1093/heapol/czu114>.
- World Health Organization. Achieving millennium development goal 5: target 5A and 5B on reducing maternal mortality and achieving universal access to reproductive health. Geneva: World Health Organization; 2009. <https://iris.who.int/handle/10665/84527>.
- GBD 2015 Maternal Mortality Collaborators. Global, regional, and national levels of maternal mortality, 1990–2015: a systematic analysis for the global burden of disease study 2015. *Lancet* 2016;388(10053):1775 – 812. [https://doi.org/10.1016/S0140-6736\(16\)31470-2](https://doi.org/10.1016/S0140-6736(16)31470-2).
- Alkema L, Chou D, Hogan D, Zhang SQ, Moller AB, Gemmill A, et al. Global, regional, and national levels and trends in maternal mortality between 1990 and 2015, with scenario-based projections to 2030: a systematic analysis by the UN maternal mortality estimation inter-agency group. *Lancet* 2016;387(10017):462 – 74. [https://doi.org/10.1016/S0140-6736\(15\)00838-7](https://doi.org/10.1016/S0140-6736(15)00838-7).
- Khalil A, Samara A, O'brien P, Coutinho CM, Quintana SM, Ladhani SN. A call to action: the global failure to effectively tackle maternal mortality rates. *Lancet Glob Health* 2023;11(8):e1165 – 7. [https://doi.org/10.1016/S2214-109X\(23\)00247-4](https://doi.org/10.1016/S2214-109X(23)00247-4).
- United Nations Maternal Mortality Estimation Inter-agency Group. Trends in maternal mortality 2000 to 2020: estimates by WHO, UNICEF, UNFPA, world bank group and UNDESA/population division. Geneva: World Health Organization. 2023. <https://iris.who.int/handle/10665/366225>.
- Ronsmans C, Graham WJ. Maternal mortality: who, when, where, and why. *Lancet* 2006;368(9542):1189 – 200. [https://doi.org/10.1016/S0140-6736\(06\)69380-X](https://doi.org/10.1016/S0140-6736(06)69380-X).
- Global Burden of Disease 2021 Health Financing Collaborator Network. Global investments in pandemic preparedness and COVID-19: development assistance and domestic spending on health between 1990 and 2026. *Lancet Glob Health* 2023;11(3):e385 – 413. [https://doi.org/10.1016/S2214-109X\(23\)00007-4](https://doi.org/10.1016/S2214-109X(23)00007-4).
- Kiernan A, Turroques L, Ahmad Y. Official development assistance trends in times of crisis. 2024. https://www.oecd.org/en/publications/2023/06/development-co-operation-profiles_17afa013/full-report/official-development-assistance-trends-in-times-of-crisis_97509fe9.html#chapter-d1e19-b5cd116b47.
- Ulrich SE, Sugg MM, Guignet D, Runkle JD. Mental health disparities among maternal populations following heatwave exposure in north Carolina (2011–2019): a matched analysis. *Lancet Reg Health Am* 2025;42:100998. <https://doi.org/10.1016/j.lana.2025.100998>.
- Strong J, Barrett R, Surtee Z, O'Hare M, Conway F, Portela A. Interventions to reduce the effects of air pollution and of extreme heat on maternal, newborn, and child health outcomes: a mapping of the literature. *J Glob Health* 2025;15:04035. <https://doi.org/10.7189/jogh.15.04035>.
- Lakhoo DP, Brink N, Radebe L, Craig MH, Pham MD, Haghghi MM, et al. A systematic review and meta-analysis of heat exposure impacts on maternal, fetal and neonatal health. *Nat Med* 2025;31(2):684 – 94. <https://doi.org/10.1038/s41591-024-03395-8>.
- Buchwald AG, Boudova S. Invited perspective: climate change and maternal mental health-looking beyond high-income countries. *Environ*

- Health Perspect 2024;132(11):111301. <https://doi.org/10.1289/EHP16476>.
22. Hanson K, Brikci N, Erlangga D, Alebachew A, De Allegri M, Balabanova D, et al. The *Lancet Global Health* commission on financing primary health care: putting people at the centre. *Lancet Glob Health* 2022;10(5):e715 – 72. [https://doi.org/10.1016/S2214-109X\(22\)00005-5](https://doi.org/10.1016/S2214-109X(22)00005-5).
23. Qiao J, Wang YY, Li XH, Jiang F, Zhang YT, Ma J, et al. A *Lancet* commission on 70 years of women’s reproductive, maternal, newborn, child, and adolescent health in China. *Lancet* 2021;397(10293):2497 – 536. [https://doi.org/10.1016/S0140-6736\(20\)32708-2](https://doi.org/10.1016/S0140-6736(20)32708-2).
24. Kruk ME, Kujawski S, Moyer CA, Adanu RM, Afsana K, Cohen J, et al. Next generation maternal health: external shocks and health-system innovations. *Lancet* 2016;388(10057):2296 – 306. [https://doi.org/10.1016/S0140-6736\(16\)31395-2](https://doi.org/10.1016/S0140-6736(16)31395-2).



Minmin Wang

Postdoctoral Research Fellow, Department of Global Health, School of Public Health, Peking University, Beijing, China



Minghui Ren

Professor, School of Public Health, Peking University, Beijing, China
Director/Chief Expert, Beijing Institute for Health Development, Peking University, Beijing, China
Director, Institute for Global Health, Peking University, Beijing, China
Director, China Center for Health Development Studies, Peking University, Beijing, China

Changing Patterns of Epidemiological Characteristics and Spatial-Temporal Clusters of Human Brucellosis Based on County Level — China, 2011–2023

Shijian Zhou¹; Huijie Qin²; Qingnan Shi¹; Sihang Li¹; Junyuan Chen²; Qiulan Chen^{1,†}

ABSTRACT

Introduction: Human brucellosis persists as a critical public health challenge in China. Understanding disease clusters and trends is essential for implementing effective control strategies. This study evaluates the epidemiological characteristics and spatiotemporal distribution of brucellosis in China from 2011 to 2023.

Methods: Data were obtained from the National Notifiable Disease Reporting System (NNDRS). We conducted descriptive epidemiological analyses and employed SaTScan10.1 and ArcGIS10.7 software to identify disease clusters and generate county (district)-level incidence maps.

Results: The incidence of human brucellosis in Chinese mainland increased substantially between 2011 and 2023, rising from 38,151 cases (2.8/100,000) across 834 counties (25.4%) to 70,439 cases (5.2/100,000) across 2,290 counties (76.9%). A significant upward trend in reported incidence emerged during 2018–2023 (average annual percentage change (AAPC)=14.9%, $P=0.01$). Most cases (89.3%) occurred in individuals aged 25–69 years, with an increasing proportion among those aged over 60 years. While 96.1% of cases were reported in northern provincial-level administrative divisions (PLADs), southern regions demonstrated escalating incidence rates and expanding geographical spread. Southern PLADs exhibited a notable annual increase of 31.5% in reported incidence ($P<0.01$). Counties (districts) with incidence rates exceeding 10 per 100,000 expanded geographically from northwestern pastoral regions to southern areas and from rural to urban settings. Primary spatiotemporal clusters were concentrated in Inner Mongolia and adjacent provincial-level administrative divisions (PLADs), with emerging clusters identified in Yunnan, Guangdong, and Xizang.

Conclusions: The human brucellosis epidemic in

China continues to intensify, characterized by rebounding incidence rates and broader geographical distribution across counties (districts). While spatiotemporal clusters remain predominantly centered in Inner Mongolia and neighboring regions, targeted interventions and increased resource allocation for high-risk areas and populations are imperative.

Brucellosis persists as one of the world's most significant “neglected zoonoses,” presenting substantial threats to human health, livestock productivity, and socioeconomic stability (1). With an annual global incidence of approximately 2.1 million cases, predominantly concentrated in Africa and Asia, the disease continues to pose a major public health challenge (2). Despite China's successful suppression of human brucellosis during the 1990s through robust preventive and control strategies, the disease has experienced a marked resurgence in the 21st century, primarily driven by expansions in the livestock industry (3). Reported cases have increased dramatically, reaching an unprecedented peak of 70,439 in 2023. The geographic distribution of the epidemic has expanded substantially, extending beyond the traditional northwestern pastoral regions such as Inner Mongolia to encompass adjacent grassland and agricultural zones with high sheep and goat populations, as well as coastal and southeastern regions (4). This evolving epidemiological landscape necessitates a comprehensive delineation of current epidemic characteristics to enhance preventive and control measures.

Spatial-temporal cluster analysis of brucellosis serves as a crucial tool for identifying and prioritizing high-risk areas for targeted interventions. Current analytical approaches typically utilize provincial-level administrative divisions, predominantly focus on northern China, or examine only short-term trends

(4–5). A significant research gap exists regarding long-term spatial and temporal patterns of brucellosis at the more granular county (district) level nationwide. To address this knowledge gap, we conducted a comprehensive examination of the epidemiological patterns and spatial-temporal distribution of human brucellosis across Chinese mainland from 2011 to 2023.

METHODS

Human brucellosis surveillance data from 31 PLADs in China (2011–2023) were obtained from the National Notifiable Disease Reporting System (NNDRS). The system incorporated both clinically diagnosed and confirmed cases based on national health industry standards. Clinically diagnosed cases were defined as presumptive cases (those with epidemiological history and clinical manifestations) with positive screening test results, while confirmed cases were defined as presumptive or clinically diagnosed cases with confirmatory experimental evidence (5). We conducted descriptive analyses following established definitions for annual incidence (AI) and regional comparisons between southern and northern regions (3). Trend analyses employed Joinpoint regression models to calculate the average annual percentage change (AAPC). Statistical analyses and disease data visualization were performed using SAS (version 9.4, SAS Institute Inc., Cary, USA) and ArcGIS Desktop (version 10.6; Esri, Redlands, California, USA).

For spatiotemporal cluster identification, we employed a Poisson retrospective spatiotemporal scan statistic using SaTScan™ software developed by Kulldorff (5). The analysis utilized a discrete Poisson distribution model to examine high spatial clustering areas across the Chinese mainland. Each scanning window was evaluated using log-likelihood ratio (LLR) and relative risk (RR) calculations to test hypotheses. The window with the maximum LLR was designated as the primary cluster, while other statistically significant windows were classified as secondary clusters (4). The analysis was conducted at the county level with daily temporal precision. The temporal aggregation period was set to 14 days, corresponding to the brucellosis incubation period. Maximum spatial and temporal window sizes were configured to encompass no more than 5% of the at-risk population

and 50% of the study duration, respectively.

RESULTS

Sociodemographic Characteristics

From 2011 to 2023, the Chinese mainland reported 656,628 cases of human brucellosis across 31 PLADs. Males were disproportionately affected, with a male-to-female ratio of 2.6:1 (475,706 males versus 180,922 females). The mean age of affected individuals was 47.59 ± 14.41 years, with 89.3% of cases occurring in those aged 25–69 years. A notable demographic shift emerged over the study period: the proportion of cases in individuals over 60 years increased annually, while the proportion in those aged 15–29 years showed a consistent decline, resulting in a net demographic shift of 7%. Throughout the study period, agricultural workers and herders constituted the predominant occupational groups affected, accounting for 82.7% to 89.7% of all cases.

Temporal Trend and Seasonality

The nationwide incidence of brucellosis demonstrated marked fluctuations throughout the study period. Reported cases increased substantially from 38,151 (2.8/100,000) in 2011 to 70,439 (5.2/100,000) in 2023, with a mean annual incidence of 3.66 per 100,000. Peak incidence occurred in 2023 at 5.0 per 100,000. A significant upward trend was observed from 2018 to 2023 (AAPC=14.9%, $P=0.01$). Southern PLADs exhibited a particularly steep increase in reported incidence from 2011 to 2023 (AAPC=31.5%, $P<0.01$). The disease demonstrated clear seasonal patterns, with 54.3% of annual cases occurring between March and July.

Spatial Characteristics

From 2011 to 2023, PLADs in northern China accounted for 96.1% of total brucellosis cases. However, PLADs in southern China exhibited a marked increase in reported cases, rising from 0.6% in 2011 to 7.4% in 2023. During this period, the geographic distribution of affected counties (districts) expanded substantially, from 834 (25.4%) in 2011 to 2,290 (76.9%) in 2023. In southern China specifically, the number of affected counties (districts) increased nearly fourfold, from 96 (9.0%) in 2011 to 932 (40.7%) in 2023 (Figure 1). Counties (districts) reporting high incidence rates exceeding 100 per 100,000 population increased from 44 (1.5%) in 2011

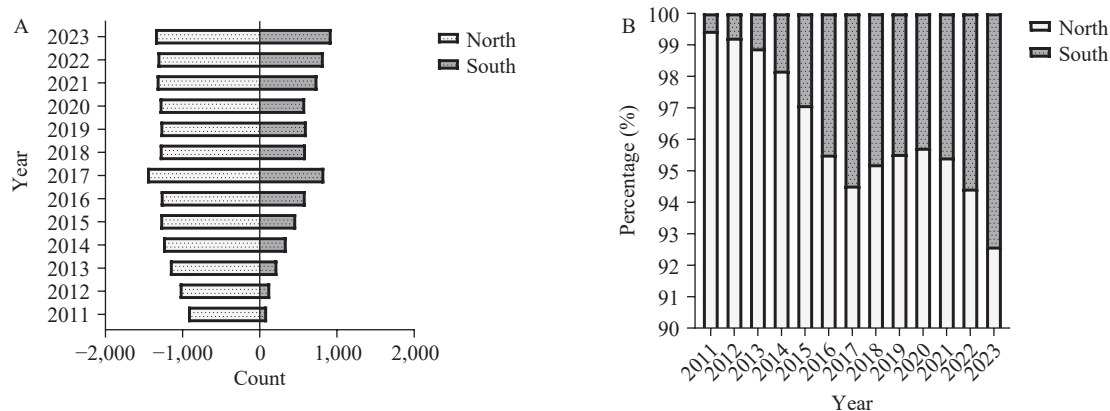


FIGURE 1. Human brucellosis in northern and southern China, 2011–2023. (A) Number of affected counties; (B) Proportion of reported cases.

to 71 (2.4%) in 2023, predominantly concentrated in northern regions, particularly Inner Mongolia and Xinjiang. Similarly, counties (districts) with incidence rates greater than 10 per 100,000 showed substantial expansion, increasing from 247 (8.4%) in 2011 to 525 (17.6%) in 2023. The geographic spread of brucellosis has demonstrated a consistent southward progression from northern China since 2013 (Figure 2 and Supplementary Table S1, available at <https://weekly.chinacdc.cn/>)

Spatial Clustering Analysis

From 2011 to 2023, we identified 227 spatiotemporal clusters of human brucellosis, comprising 13 primary and 214 secondary clustering areas. The primary clusters initially centered in eastern Inner Mongolia before progressively expanding to encompass eight adjacent PLADs (Heilongjiang, Jilin, Liaoning, Hebei, Shanxi, Shaanxi, Ningxia, Gansu) and part regions in Xinjiang. This expansion pattern persisted throughout the study period. Notably, in 2015–2016, novel clusters emerged in southern PLADs, specifically affecting Guangdong, Hubei, and Guangxi (Supplementary Tables S2–S3, available at <https://weekly.chinacdc.cn/>). By 2017, the disease had spread to 183 counties (districts), predominantly concentrated in northern PLADs including Shanxi, Inner Mongolia, Heilongjiang, Xinjiang, Hebei, Liaoning, Gansu, and Shandong, with Xizang reporting secondary clusters for the first time (Supplementary Tables S2–S3). The period between 2018 and 2021 saw a reduction in affected counties, with clusters reconcentrating in Inner Mongolia and adjacent PLADs. While clusters in Yunnan persisted from 2019 onward, Xinjiang ceased reporting clusters

from 2020. Re-emergence of spatiotemporal clusters in Xinjiang in 2023. In 2022–2023, there was a resurgence in affected counties, primarily in the Inner Mongolia and its surrounding eight PLADs, as well as in Shandong, Henan, Qinghai, and Xinjiang PLADs. The temporal evolution of primary clustering showed distinct geographical shifts: from 2011 to 2014, it was predominantly in eastern Inner Mongolia and neighboring PLADs such as Heilongjiang and Jilin; from 2015 to 2017, it shifted to the western Inner Mongolia and expanded to Xinjiang, Ningxia, and other regions; from 2018 to 2021, it returned to eastern Inner Mongolia; from 2022 to 2023, shifted to western Inner Mongolia as well as Shanxi, Shaanxi, Ningxia, Gansu, Qinghai and Xinjiang regions (Figure 3). Among the 227 spatiotemporal clusters identified, primary clusters occurred predominantly from February to August, while secondary clusters spanned January to July (Table 1).

DISCUSSION

This study reveals significant shifts in the epidemiological landscape and spatiotemporal distribution of brucellosis across China from 2011 to 2023. Our findings demonstrate the persistent severity of the epidemic, characterized by both a resurgence in reported cases and substantial geographic expansion across counties (districts). The disease pattern has evolved from its initial concentration in northern pastoral provinces to encompass adjacent grassland and agricultural regions, ultimately extending into southern coastal and southwestern areas. Spatiotemporal analysis revealed distinct clustering patterns, with primary hotspots centered in Inner Mongolia and traditional

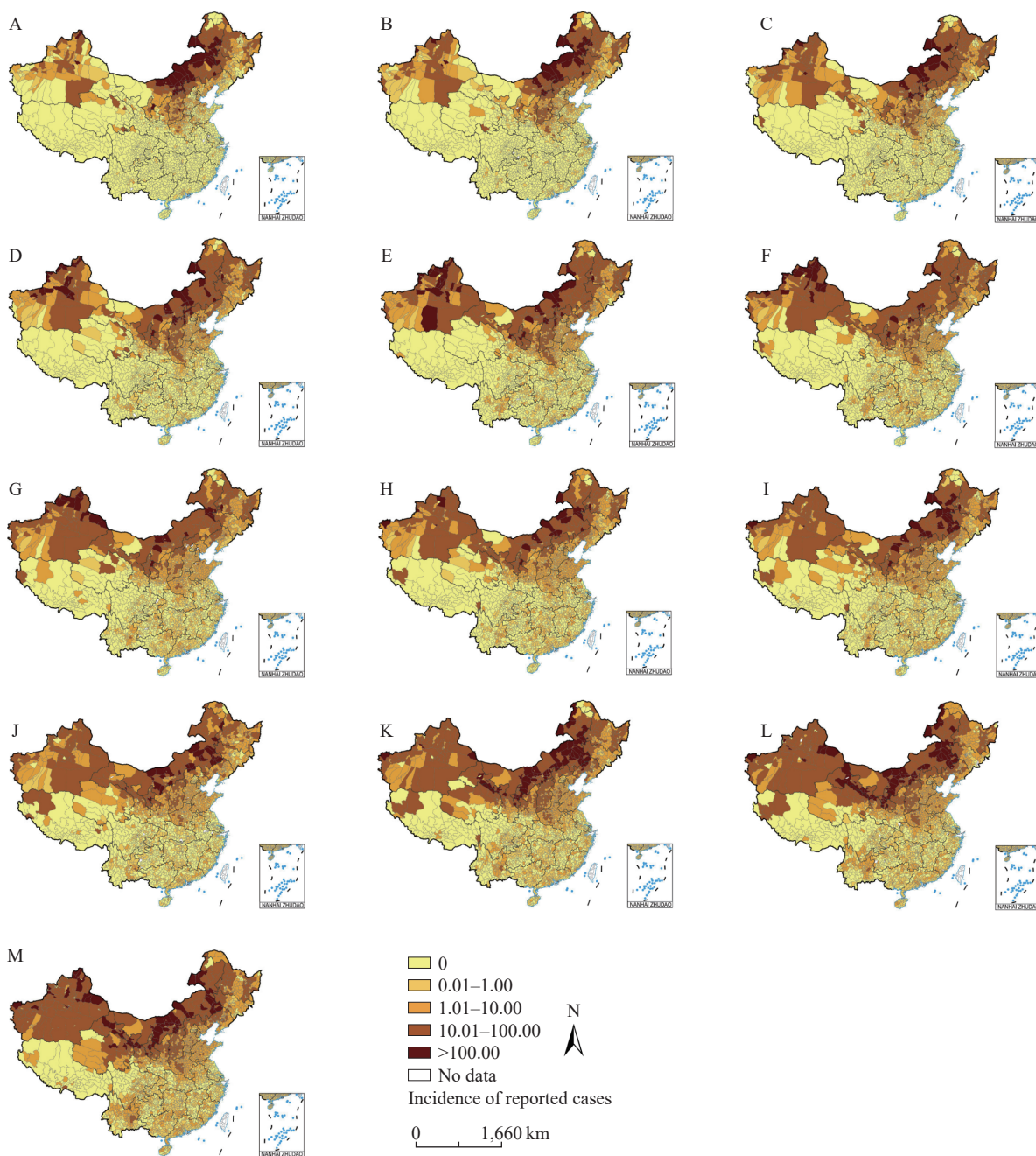


FIGURE 2. Geographical distribution of incidence of the reported human brucellosis in 31 PLADs of China, 2011–2023. (A)–(M) From 2011 to 2023.

Abbreviation: PLAD=provincial-level administrative division.

Map approval number: GS 京 (2025)0527 号.

pastoral regions of western and northeastern China. Throughout the 13-year study period, the disease exhibited a clear eastward-to-westward progression within Inner Mongolia, subsequently spreading to adjacent PLADs and part regions in Xinjiang. A particularly noteworthy development since 2019 has been the emergence of new hotspots in the southern PLAD of Yunnan, demanding immediate attention

from public health authorities. In 2023, many hotspots appeared in Xinjiang and Qinghai, which may be related to its improved ability to detect brucellosis.

The age distribution analysis reveals a concerning trend: the proportion of infections among individuals over 60 years has shown consistent annual increases. This demographic shift likely reflects the aging population structure among Chinese farmers and

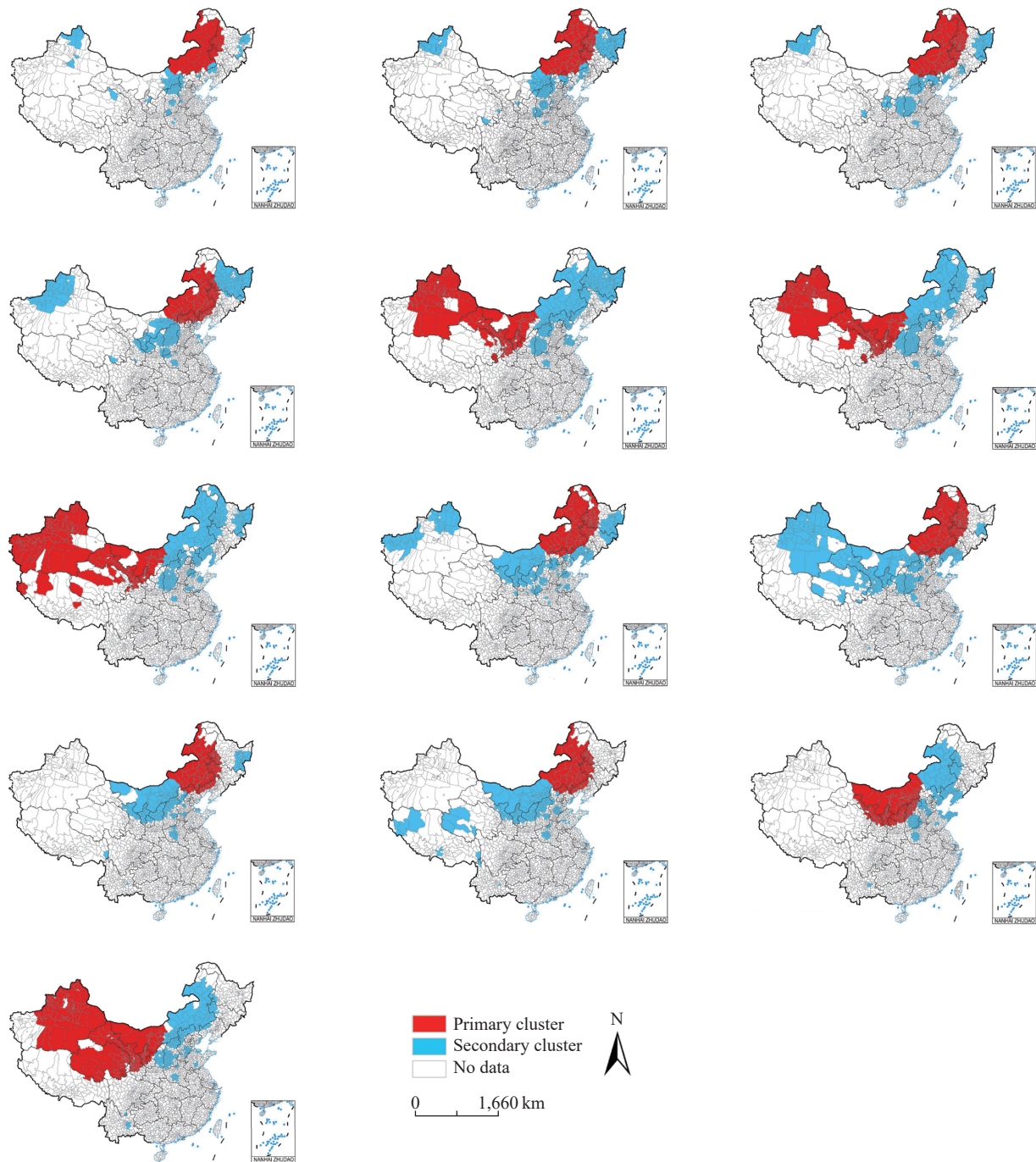


FIGURE 3. Spatial clustering of the reported brucellosis cases in 31 PLADs of China, 2011–2023. (A)–(M) From 2011 to 2023.

Abbreviation: PLAD=provincial-level administrative division.

Map approval number: GS 京 (2025)0527 号.

herders engaged in livestock management (5). This finding underscores the urgent need for targeted health education initiatives specifically designed for this vulnerable age group.

The rising incidence of human brucellosis in China, particularly in southern regions, can be attributed to

several interconnected factors. First, there exists a robust positive correlation between human brucellosis incidence and livestock outbreak frequency (6–7). Despite persistent and intensifying animal outbreaks, preventive measures — including livestock vaccination programs and quarantine protocols — have proven

TABLE 1. Spatiotemporal clusters of human brucellosis in China, 2011–2023.

Scan time frame (year)	Cluster time (mm/dd–mm/dd)	Centroid (latitude, longitude)/radius (km)	Cluster counties (n)	LLR	RR	P
2011	2/13–8/13	(48.6N, 116.8E)/715.6	78	16,848.2	15.2	<0.001
2012	1/31–7/30	(48.6N, 116.8E)/737.0	87	17,093.2	15.0	<0.001
2013	1/1–7/2	(48.6N, 116.8E)/780.7	104	11,305.8	10.2	<0.001
2014	1/1–7/2	(45.7N, 117.0E)/605.8	125	11,444.6	8.4	<0.001
2015	3/13–9/10	(43.5N, 95.0E)/1280.0	159	9,979.3	7.9	<0.001
2016	2/28–8/27	(43.5N, 95.0E)/1281.8	161	10,097.4	9.4	<0.001
2017	2/13–8/13	(48.3N, 87.2E)/2003.2	183	6,752.9	7.9	<0.001
2018	2/27–8/27	(48.6N, 116.8E)/809.3	117	9,690.0	11.1	<0.001
2019	2/13–8/13	(48.6N, 116.8E)/809.3	118	13,780.5	13.1	<0.001
2020	2/28–8/27	(45.7N, 118.8E)/530.6	109	14,367.6	13.5	<0.001
2021	1/30–7/30	(45.7N, 118.8E)/530.6	109	18,540.7	13.9	<0.001
2022	2/27–8/27	(41.5N, 106.4E)/644.0	159	24,912.4	15.3	<0.001
2023	2/27–8/27	(43.6N, 94.9E)/1312.2	223	20231.2	10.9	<0.001

Abbreviation: LLR=log likelihood ratio; RR=relative risk.

insufficient (4,8). Recent surveillance data indicate elevated seroprevalence rates among dairy cattle and sheep populations (9–10). Second, the surge in livestock product demand has intensified north-to-south animal transportation, exacerbating the epidemic's spread to southern regions (4,8). Third, inadequate regional quarantine measures and limited stakeholder awareness of quarantine protocols have contributed to outbreaks in southern China, as evidenced by cases linked to sika deer and raw goat milk consumption (11–12). Furthermore, the diversification of livestock production systems — encompassing free-range, grazing, and intensive production methods — has complicated disease prevention and control efforts (10,13).

The spatial-temporal clustering patterns of human brucellosis have aligned with broader epidemic trends, with Inner Mongolia and adjacent regions remaining critical focal points. Molecular epidemiological studies have revealed genetic homology between *Brucella* strains isolated from northern provinces, including Xinjiang and Inner Mongolia (14), and those found in Shanxi and neighboring provinces (15). This genetic relationship underscores the need for enhanced quarantine measures and stringent management of livestock and dairy product movement between high-incidence regions to curtail disease transmission. In Yunnan, the rapid emergence of brucellosis cases, potentially linked to expanding dairy goat operations, necessitates the implementation of prevention and control strategies specifically tailored to local livestock

industry developments.

Despite the implementation of the National Brucellosis Prevention and Control Plan (2016–2020) (NBPCP), brucellosis incidence rates have continued their upward trajectory. In response, brucellosis was designated as a priority disease for prevention and control in 2022. This designation necessitates comprehensive animal-based prevention and control strategies from governmental bodies at all levels, encompassing immunization, quarantine, and culling protocols. Furthermore, there is an urgent need to strengthen occupational safety measures for at-risk populations to reduce both inter-animal transmission and occupational exposure, thereby mitigating the disease's escalating impact on human populations. Additionally, management approaches should be tailored to regional specificities, with enhanced oversight in high-risk areas. While this study presents a spatial-temporal aggregation analysis at the district-county scale, future research could explore patterns at smaller administrative levels, such as townships, to provide more granular insights for precise prevention and control strategies.

This study has several limitations. First, county codes for a small proportion (<10%) of cases could not be matched with the corresponding map dataset, though this discrepancy is minor and does not significantly impact the data's representativeness. Additionally, the reported case numbers may underestimate the true disease burden due to inherent limitations in surveillance data.

Conflicts of interest: No conflicts of interest.

Funding: Supported by the Public Health Emergency Response Mechanism Operation Program of Chinese Center for Disease Control and Prevention (102393220020010000017).

doi: 10.46234/ccdcw2025.075

Corresponding author: Qiulan Chen, chenql@chinacdc.cn.

¹ National Key Laboratory of Intelligent Tracking and Forecasting for Infectious Diseases, Chinese Center for Disease Control and Prevention, Beijing, China; ² School of Public Health, Guangxi Medical University, Nanning City, Guangxi Zhuang Autonomous Region, China.

Copyright © 2025 by Chinese Center for Disease Control and Prevention. All content is distributed under a Creative Commons Attribution Non Commercial License 4.0 (CC BY-NC).

Submitted: November 20, 2024

Accepted: March 25, 2025

Issued: April 04, 2025

REFERENCES

- Lai SJ, Chen QL, Li ZJ. Human brucellosis: an ongoing global health challenge. *China CDC Wkly* 2021;3(6):120 – 3. <https://doi.org/10.46234/ccdcw2021.031>.
- Laine CG, Johnson VE, Scott HM, Arenas-Gamboa AM. Global estimate of human brucellosis incidence. *Emerg Infect Dis* 2023;29(9):1789 – 97. <https://doi.org/10.3201/eid2909.230052>.
- Tao ZF, Chen QL, Chen YS, Li Y, Mu D, Yang HM, et al. Epidemiological characteristics of human brucellosis - China, 2016-2019. *China CDC Wkly* 2021;3(6):114 – 9. <https://doi.org/10.46234/ccdcw2021.030>.
- Yang HM, Chen QL, Li Y, Mu D, Zhang YP, Yin WW. Epidemic characteristics, high-risk areas and space-time clusters of human brucellosis - China, 2020-2021. *China CDC Wkly* 2023;5(1):17 – 22. <https://doi.org/10.46234/ccdcw2023.004>.
- Liang PF, Zhao Y, Zhao JH, Pan DF, Guo ZQ. Human distribution and spatial-temporal clustering analysis of human brucellosis in China from 2012 to 2016. *Infect Dis Poverty* 2020;9(1):142. <https://doi.org/10.1186/s40249-020-00754-8>.
- Wang Y, Wang Y, Zhang LN, Wang AP, Yan Y, Chen YY, et al. An epidemiological study of brucellosis on Chinses mainland during 2004-2018. *Transbound Emerg Dis* 2021;68(4):2353 – 63. <https://doi.org/10.1111/tbed.13896>.
- Zhang D, Lv DY, Zheng XJ, Duan R, Qin S, Lu XM, et al. Case report: screening and analysis for brucellosis in Akesai Kazak autonomous county, China. *Am J Trop Med Hyg* 2023;108(6):1201 – 3. <https://doi.org/10.4269/ajtmh.22-0802>.
- Li Y, Tan D, Xue S, Shen CJ, Ning HJ, Cai C, et al. Prevalence, distribution and risk factors for brucellosis infection in goat farms in Ningxiang, China. *BMC Vet Res* 2021;17(1):39. <https://doi.org/10.1186/s12917-021-02743-x>.
- Ran XH, Cheng JJ, Wang MM, Chen XH, Wang HX, Ge Y, et al. Brucellosis seroprevalence in dairy cattle in China during 2008-2018: a systematic review and meta-analysis. *Acta Trop* 2019;189:117 – 23. <https://doi.org/10.1016/j.actatropica.2018.10.002>.
- Li LM, Wang Q, Shi JF, Li T, Zhao B, Ma QX, et al. Seroprevalence and potential risk factors of brucellosis in sheep from America, Africa and Asia regions: a systematic review and meta-analysis. *Res Vet Sci* 2023;165:105048. <https://doi.org/10.1016/j.rvsc.2023.105048>.
- Tao ZF, Yang ZP, Chen YS, Yang SF, Xu JC, Wang Y, et al. Epidemiological survey of first human brucellosis outbreak caused by the sika deer (*Cervus nippon*) - Guizhou Province, China, 2019. *China CDC Wkly* 2021;3(14):301 – 3. <https://doi.org/10.46234/ccdcw2021.081>.
- Di M, Tao ZF, Hua WP, Chen JD, Cao JM, Deng YQ, et al. Investigation of brucellosis caused by raw goat milk - Fujian Province, China, April-June, 2019. *China CDC Wkly* 2021;3(20):430 – 3. <https://doi.org/10.46234/ccdcw2021.111>.
- An CH, Shen L, Sun MH, Sun YX, Fan SP, Zhao CX, et al. Exploring risk transfer of human brucellosis in the context of livestock agriculture transition: a case study in Shaanxi, China. *Front Public Health* 2022;10:1009854. <https://doi.org/10.3389/fpubh.2022.1009854>.
- Zhang H, Deng XY, Cui BY, Shao ZR, Zhao XL, Yang Q, et al. Abortion and various associated risk factors in dairy cow and sheep in Ili, China. *PLoS One* 2020;15(10):e0232568. <https://doi.org/10.1371/journal.pone.0232568>.
- An CH, Nie SM, Sun YX, Fan SP, Luo BY, Li ZJ, et al. Seroprevalence trend of human brucellosis and MLVA genotyping characteristics of *Brucella melitensis* in Shaanxi Province, China, during 2008-2020. *Transbound Emerg Dis* 2022;69(4):e423 – 34. <https://doi.org/10.1111/tbed.14320>.

SUPPLEMENTARY MATERIAL

SUPPLEMENTARY TABLE S1. Number of affected counties with different incidence levels in China, 2011–2023.

Year	Total number of counties	Incidence (1/100,000) of affected counties									
		0		0.01–1		1.01–10		10.01–100		100.01–	
		N	Prevalence (%)*	N	Prevalence (%)*	N	Prevalence (%)*	N	Prevalence (%)*	N	Prevalence (%)*
2011	2,958	1,932	65.31	372	12.58	407	13.76	203	6.86	44	1.49
2012	2,974	1,800	60.52	433	14.56	440	14.79	264	8.88	37	1.24
2013	2,935	1,543	52.57	505	17.21	540	18.40	314	10.70	33	1.12
2014	2,938	1,334	45.41	537	18.28	643	21.89	373	12.70	51	1.74
2015	2,946	1,184	40.19	611	20.74	711	24.13	397	13.48	43	1.46
2016	2,945	1,068	36.26	702	23.84	782	26.55	361	12.26	32	1.09
2017	2,948	1,005	34.09	802	27.20	813	27.58	309	10.48	19	0.64
2018	2,949	1,054	35.74	777	26.35	804	27.26	293	9.94	21	0.71
2019	2,947	1,049	35.60	742	25.18	815	27.66	309	10.49	31	1.05
2020	2,958	1,070	36.17	712	24.07	832	28.13	310	10.48	34	1.15
2021	2,976	893	30.01	721	24.23	845	28.39	452	15.19	65	2.18
2022	2,901	745	25.68	800	27.58	871	30.02	415	14.31	70	2.41
2023	2,978	688	23.10	803	26.96	962	32.30	454	15.25	71	2.38

Abbreviation: N=number of counties.

* Percentage of the counties.

SUPPLEMENTARY TABLE S2. Number of districts and counties involved in the primary clusters of brucellosis in China, 2011–2023.

Province	Year												
	2011	2012	2013	2014	2015	2016	2017	2018	2019	2020	2021	2022	2023
Inner Mongolia	41	45	51	55	22	24	25	54	55	48	48	56	29
Heilongjiang	31	32	41	13	0	0	0	44	44	21	21	0	0
Xinjiang	0	0	0	0	68	66	91	0	0	0	0	0	75
Gansu	0	0	0	0	43	45	38	0	0	0	0	26	54
Jilin	6	9	10	9	0	0	0	12	12	14	14	0	0
Ningxia	0	0	0	0	18	18	16	0	0	0	0	20	21
Liaoning	0	0	0	22	0	0	0	2	2	21	21	0	0
Hebei	0	1	2	25	0	0	0	5	5	5	5	0	0
Shanxi	0	0	0	0	0	0	0	0	0	0	0	35	0
Qinghai	0	0	0	0	7	7	9	0	0	0	0	2	42
Shaanxi	0	0	0	0	1	1	0	0	0	0	0	20	1
Xizang	0	0	0	0	0	0	4	0	0	0	0	0	1

SUPPLEMENTARY TABLE S3. Number of districts and counties involved in the secondary clusters of brucellosis in China, 2011–2023.

Province	Year												
	2011	2012	2013	2014	2015	2016	2017	2018	2019	2020	2021	2022	2023
Shanxi	53	78	87	97	93	116	96	62	89	51	53	48	79
Heilongjiang	17	76	51	107	121	93	93	47	17	36	0	20	9
Inner Mongolia	29	37	16	28	65	65	70	42	40	54	55	43	67
Hebei	16	28	32	9	51	38	71	50	37	31	43	73	63
Liaoning	7	13	19	0	18	16	46	70	73	0	0	68	4
Henan	3	7	13	25	25	19	11	7	17	37	37	36	24
Shandong	1	1	0	7	34	42	38	31	14	4	8	34	12
Xinjiang	12	20	21	42	0	0	0	49	68	0	0	0	0
Shaanxi	1	7	27	23	15	23	15	26	34	20	20	0	21
Gansu	0	0	1	18	0	0	0	18	48	14	15	0	0
Ningxia	2	1	8	18	0	0	0	20	19	20	20	0	0
Jilin	0	1	2	3	17	11	12	10	0	0	0	10	7
Qinghai	1	2	2	1	0	0	0	0	23	0	3	0	0
Beijing	0	2	3	0	2	2	1	2	2	1	0	1	0
Xizang	0	0	0	0	0	0	0	0	0	1	9	0	0
Yunnan	0	0	0	0	0	0	0	0	1	1	2	3	6
Tianjin	0	0	1	0	0	1	1	0	0	0	0	0	0
Guangdong	0	0	0	0	1	0	0	0	1	0	0	0	0
Hubei	0	0	0	0	0	1	0	0	0	0	0	0	0
Guangxi	0	0	0	0	0	1	0	0	0	0	0	0	0
Sichuan	0	0	0	0	0	0	0	0	0	0	0	0	1

Vital Surveillances

Epidemiological Evolution Profile of Human Brucellosis and Socioeconomic Factor Correlation Analysis — Southern and Northern Areas, China, 1950–2021

Zhiguo Liu¹; Miao Wang²; Yue Shi³; Liping Wang³; Xiang Ren³; Zhenjun Li^{3, #}; Canjun Zheng^{3, #}

ABSTRACT

Introduction: Human brucellosis poses a serious public health concern in China, however, epidemiological evolution of disease in southern and northern China remains unclear.

Methods: The number of cases, incidence rate, geographic and temporal distribution, and social factors were analyzed to illustrate the epidemiological change.

Results: About 97.6% of cases consistently located in the northern area are attributed to the tens of thousands of livestock farming. This underscores the need to prioritize strengthening surveillance and control measures in the northern. By contrast, only 2.4% of cases were in the southern area. These data indicate that controlling brucellosis in the northern will help reduce the incidence in the southern. There was an apparent shift from historical multiple-species prevalence to the present dominance of a single species, *Brucella melitensis*. Mutton price and production were closely correlated with the number of cases, implying that *B. melitensis* strains were accompanied by these factors, co-driving the persistent epidemic of brucellosis and expanding from the northern toward the southern.

Conclusions: The control and prevention of brucellosis in the northern have become extremely complex sociological issues. It is important to draw attention to the worsening epidemic situation and to mobilize the nation's full strength to curb this trend.

Brucellosis is a globally distributed zoonotic disease that causes substantial economic losses in agriculture and poses a significant public health concern worldwide (1). Human brucellosis cases have been documented across all 31 provincial-level administrative divisions (PLADs) in China (2). Case

numbers have shown continuous growth in recent years, driven by multiple socioeconomic factors, particularly the expansion of sheep and goat livestock industries and increased economic development (3). Understanding the epidemiological change between southern and northern areas is therefore crucial for developing targeted and effective control measures. This study aims to elucidate the epidemiological evolutionary characteristics of human brucellosis and examining the relationships among multiple contributing social factors. These insights will contribute to the development of tailored countermeasures to combat the spread of brucellosis.

METHODS

The Qinling-Huaihe Line served as the geographical demarcation between northern and southern areas China, encompassing 16 northern PLADs and 15 southern PLADs. Case numbers and incidence rates were obtained from the National Information System for Disease Control and Prevention of China and the China Health Statistical Yearbook. Economic indicators were sourced from the National Bureau of Statistics (<http://www.stats.gov.cn/>) (Supplementary Table S1, available at <https://weekly.chinacdc.cn/>). The geographic distribution and biotype profiles of 1,643 *Brucella* strains documented from 1950 to 2016 were compiled from previously published sources (4), while subsequent strain data from 2017 to 2021 were extracted from annual infectious disease surveillance reports in China.

Data processing and analysis were performed using Excel 2016 (Microsoft, Redmond, WA, USA). A heatmap was generated using an online data analysis pipeline (<https://www.chiplot.online/#Line-plot>), and disease growth trends were visualized using semilogarithmic curves. Correlation analysis was performed using Pearson's correlation coefficient by R Studio (Ross Ihaka and Robert Gentleman, Boston, MA, United States).

RESULTS

The epidemic evolution of human brucellosis can be categorized into three distinct phases: 1) severe epidemic period (1950–1985), 2) primary control period (1986–1995), and 3) continuous increase period (1996–present). The reported case progression demonstrates a clear transmission pattern: originating in the northeast, spreading northward, then moving southwest, and ultimately reaching China's southern most point — Hainan Island (Figure 1). The number of reported cases has increased dramatically, from 8 in 1950 to 69,767 in 2021, with the incidence rate rising from 0.002/100,000 to 4.949/100,000 during this period (Figure 1).

Out of the 815,347 reported cases, 796,987 (97.7%) occurred in the northern, while only 18,360 (2.3%) were reported in the southern. Although the southern has experienced a considerable increase in cases since 2010, the northern continues to bear the majority of cases (Figure 2). The incidence rate of human brucellosis in the southern remained below 0.463/100,000 in 2015 and 1.485/100,000 in 2021 (Supplementary Table S1).

From 2000 to 2021, both the fixed base ratio growth rate of cases and incidence rate showed a consistent upward trend nationally, while the sequential growth rate exhibited an initial increase followed by a decrease and subsequent increase (Table 1). A parallel pattern emerged between northern and southern regions, where the fixed base ratio growth rate maintained steady increases, while the sequential

growth rate fluctuated between periods of growth and decline.

The period between 2011 and 2021 represented the peak of reported cases, accounting for 63.6% (520,197/818,413) of all documented incidents. This was followed by the periods 2001–2010, 1961–1970, and 1971–1980 (Figure 3A). The lowest case numbers were recorded during 1991–2000 (Figure 3A). At the provincial level, the number of cases can be stratified into four distinct ranks (I–IV). Rank I comprises solely Inner Mongolia, which reported the highest number of cases in mainland China, representing 37.6% (307,595/818,413) of total cases. Rank II encompasses five northern PLADs, while rank III includes six PLADs. Rank IV, representing the lowest case numbers, consists of all southern PLADs (Figure 3A). While approximately 98% of the reported cases were concentrated in the northern, the Southern experienced a notable increase in case reports from 2014 onward.

The seasonal distribution patterns show a remarkable similarity between northern and southern regions, with case numbers reaching a peak in May and trough in November across both areas (Figure 3B). The seasonal distribution of cases can be categorized into three distinct groups: group A, spanning March to July, exhibits the highest number of reported cases; group B, encompassing January, February, and August, shows intermediate levels; and group C, extending from September to December, demonstrates the lowest case numbers (Figure 3B).

Analysis of 2,787 *Brucella* strains isolated between 1950 and 2021. While *B. melitensis* and *B. abortus*

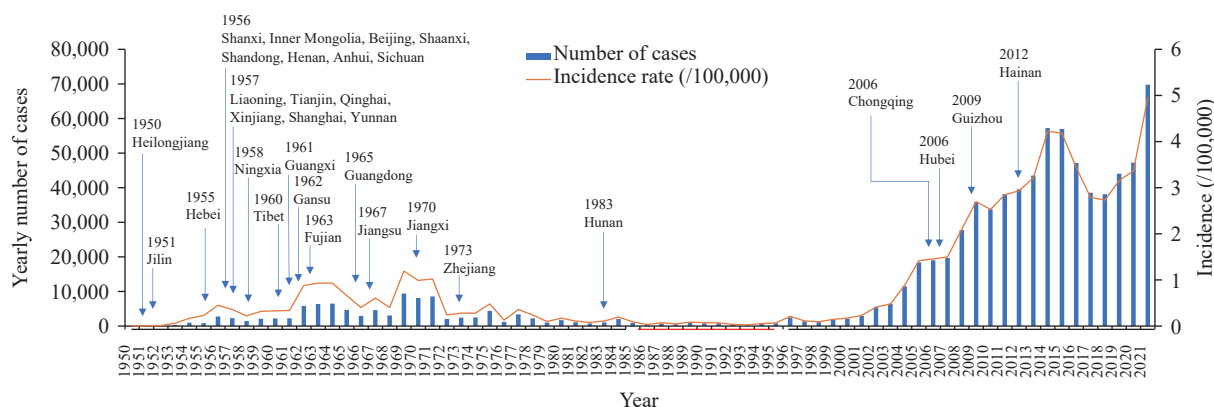


FIGURE 1. The changing trend of reported cases and incidence rate of human brucellosis from 1950–2021.

Note: Blue arrow indicates the first reported case of human brucellosis in each PLAD or region. The bold black line parallel to the X-axis represents the duration of two epidemic periods, and the bold red line indicates the duration of the control period of human brucellosis in China.

Abbreviation: PLAD=provincial-level administrative division.

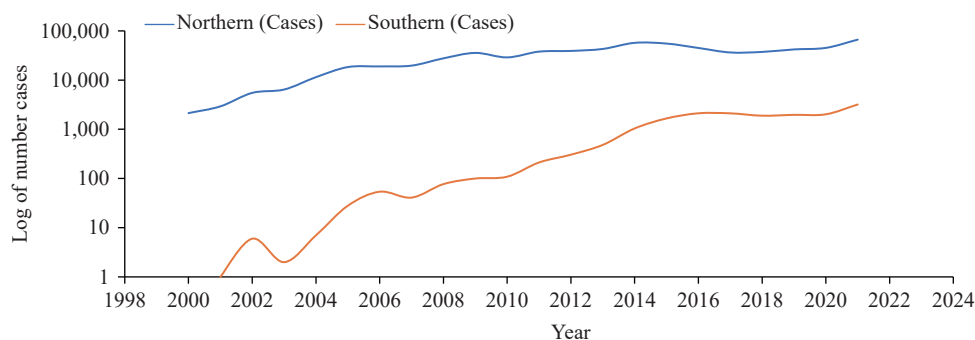


FIGURE 2. Growth trends of human brucellosis between northern and southern China.

Note: There were no reported cases from Hong Kong SAR; Macao SAR; and Taiwan, China; the incidence rate in these three regions was 0/100,000.

Abbreviation: SAR=Special Administrative Region.

TABLE 1. Epidemic growth trends of cases and incidence from 2000 to 2021.

Year	Number of cases			Incidence rate (/100 000)		
	Cases	Fixed base ratio growth rate (%)	Sequential growth rate (%)	Incidence (/100 000)	Fixed base ratio growth rate (%)	Sequential growth rate (%)
2000	2,126	–	–	0.171	–	–
2001	2,918	37.25	37.25	0.229	34.03	34.03
2002	5,505	158.94	88.66	0.411	139.99	79.05
2003	6,448	203.29	17.13	0.478	179.16	16.32
2004	11,472	439.60	77.92	0.882	415.18	84.55
2005	18,416	766.23	60.53	1.416	727.03	60.53
2006	19,013	794.31	3.24	1.454	748.86	2.64
2007	19,721	827.61	3.72	1.500	775.83	3.18
2008	27,767	1,206.07	40.80	2.101	1,126.80	40.07
2009	35,816	1,584.67	28.99	2.696	1,474.37	28.33
2010	33,772	1,488.52	–5.71	2.530	1,377.06	–6.18
2011	38,151	1,694.50	12.97	2.845	1,560.95	12.45
2012	39,515	1,758.65	3.58	2.933	1,612.08	3.08
2013	43,486	1,945.44	10.05	3.212	1,774.84	9.51
2014	57,222	2,591.53	31.59	4.223	2,364.97	31.48
2015	56,989	2,580.57	–0.41	4.183	2,341.80	–0.94
2016	47,139	2,117.26	–17.28	3.439	1,907.47	–17.79
2017	38,554	1,713.45	–18.21	2.794	1,531.12	–18.75
2018	39,296	1,748.35	1.92	2.829	1,551.43	1.25
2019	44,036	1,971.31	12.06	3.153	1,740.75	11.46
2020	47,245	2,122.25	7.29	3.365	1,864.62	6.73
2021	69,767	3,181.61	47.67	4.949	2,788.97	47.05

were predominantly distributed in the northern, *B. suis* and *B. canis* strains were primarily found in the southern. Notably, *B. melitensis* has emerged as the dominant species nationwide, with substantial isolates recovered from southern PLADs, including Guangdong, Zhejiang, and Hainan. *B. abortus* strains

were predominantly isolated from Inner Mongolia and Sichuan PLADs, while *B. suis* strains were distributed across Inner Mongolia, Ningxia, Guangxi, Guangdong, and Hainan. On its part, *B. canis* strains were primarily isolated from Beijing, Jiangsu, and Guangxi. There was a clear transition from multiple

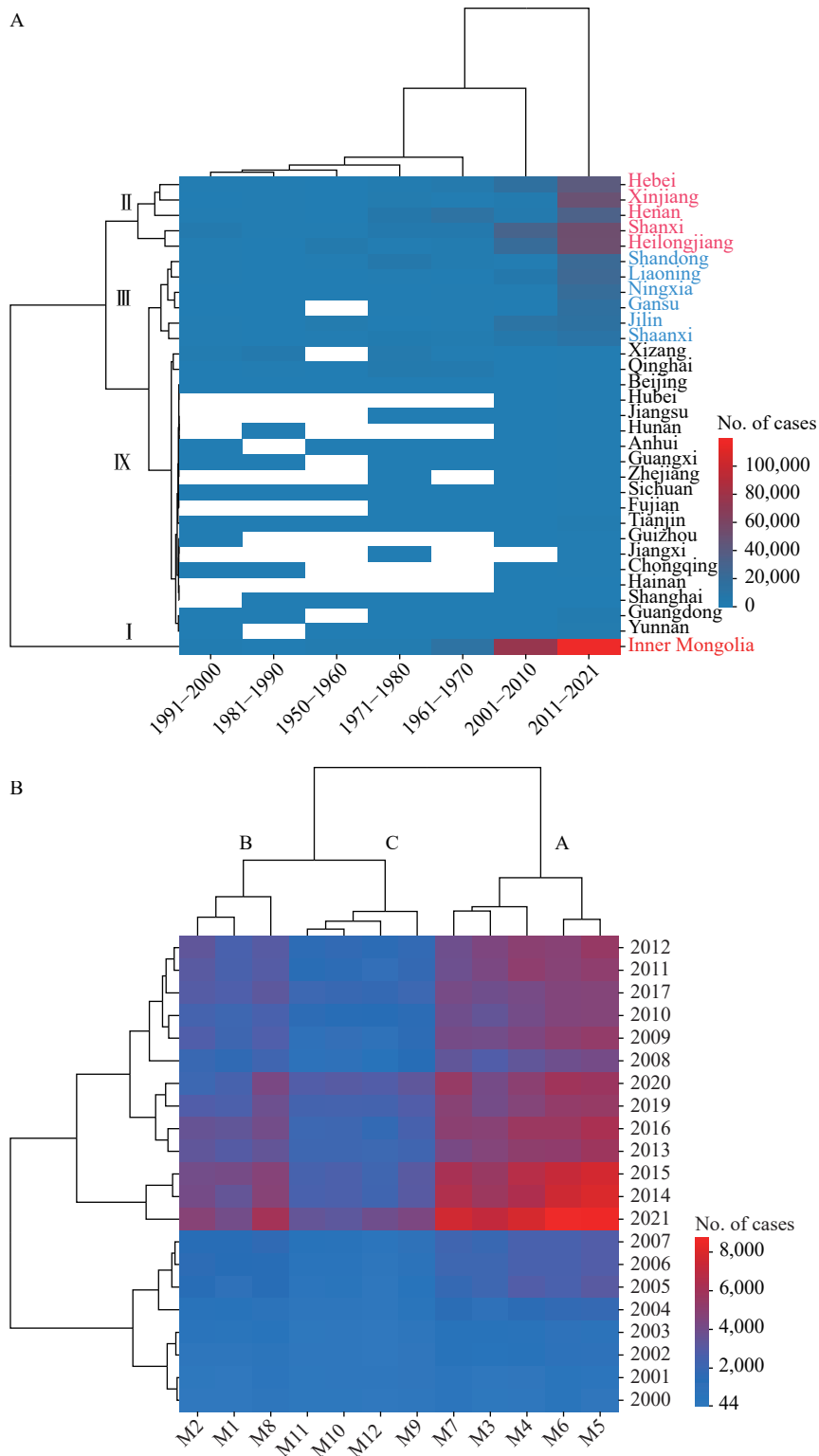


FIGURE 3. Distribution features of human brucellosis in northern and southern China. (A) Time and regions; (B) seasonal distribution.

dominant species before 2000 to the current single predominance of *B. melitensis* (Figure 4).

Correlation analysis revealed significant associations

between human brucellosis cases, multiple animal husbandry and economic factors (Figure 5), including mutton price ($R=0.91$), followed by mutton

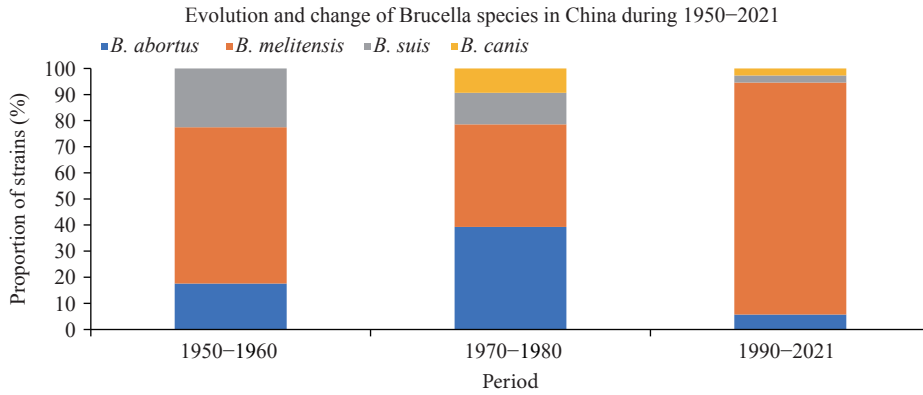


FIGURE 4. Species/biotype change trends of *Brucella* strains in China.

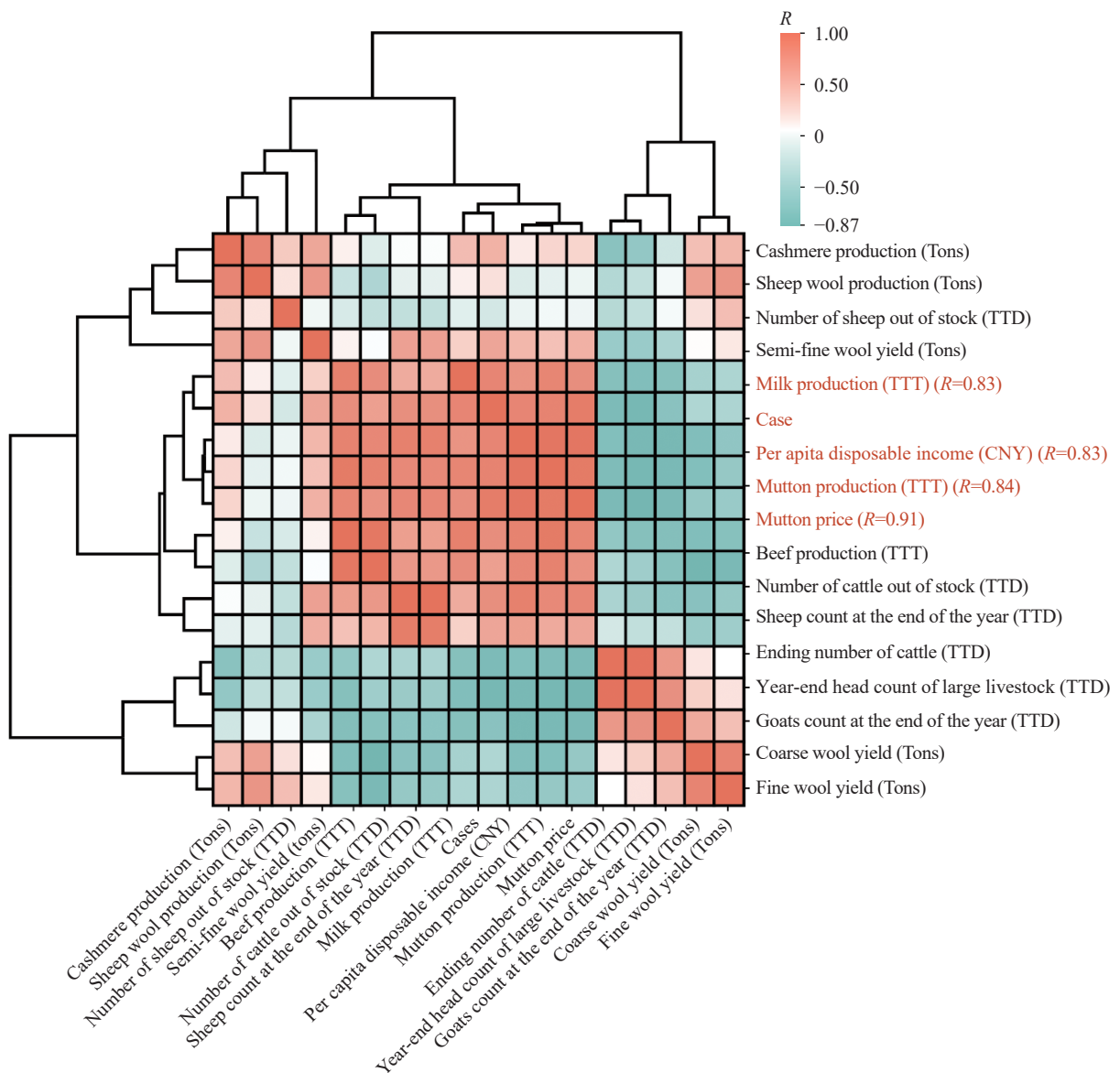


FIGURE 5. Correlation analysis of reported cases and incidence rate (Supplementary Figure S1, available at <https://weekly.chinacdc.cn/>) of human brucellosis and animal husbandry factors.

Abbreviation: TTD=Ten thousand heads; TTT=Ten thousand tons; CNY=Chinese Yuan.

production ($R=0.84$), milk production ($R=0.83$), per capita disposable income ($R=0.83$), beef production ($R=0.77$) and end-of-year sheep and goat counts ($R=0.75$) (Figure 5 and Supplementary Table S2, available at <https://weekly.chinacdc.cn/>).

DISCUSSION

Our analysis reveals a three-phase progression of human brucellosis in China, characterized by an initial epidemic from 1950–1985, a control period from 1986 to 1995, and disease re-emergence from 1996 to 2021. Due to mass animal vaccination campaigns implemented in the late 1970s, the *Brucella* infection rate decreased to 0.3% in humans and 0.5%–1.0% in animals. Since 1995, human brucellosis has re-emerged as an epidemic disease in China, driven by multiple policy and technical factors. Notably, there has been an increased socioeconomic development alongside persistent lifestyle farming practices. These findings emphasize the crucial importance of maintaining continuous surveillance and intervention measures, even during periods of low disease incidence, to prevent epidemic re-emergence.

High-incidence clusters are predominantly located in northeastern China, while low-incidence clusters are concentrated in southern regions (5). Traditional farming practices, driven by profit maximization in limited spaces often lead to the import of infected animals, and increased abortion rates. This results in frequent human-animal contact and an increased infection risk. The prevalence of small, individually operated farms leads to arbitrary implementation of epidemic prevention measures, resulting in inadequate detection and vaccination protocols, insufficient compensation mechanisms, and continued circulation of infected animals in the market (6).

In the southern, Guangdong and Yunnan provinces reported the highest case numbers and incidence rates. This means that southern cases had minimal impact on the overall endemic progression for nearly two decades, suggesting that controlling brucellosis in the Northern would contribute to a decreased southern incidence. For the southern, recommended strategies include strengthened inspection and quarantine of imported animals and their byproducts, alongside enhanced disease intervention in high-risk populations.

This study has shown that the mutton price, mutton production, milk production, and per capita disposable income are significantly correlated with high brucellosis incidence. Sheep inventory, gross domestic

product (GDP), and climate have also been significantly associated with human brucellosis incidence in China (7). A clear relationship exists between disease status and economic resources: countries with higher GDP per capita tend to be free from bovine brucellosis (8). Regions characterized by larger sheep and cattle populations, lower GDP per capita, higher wind speeds, and lower mean temperatures are more likely to become high-risk areas (9).

The control and prevention of human brucellosis require long-term investment and systematic multi-sectoral cooperation. Although animal vaccination represents the most cost-effective control measure with demonstrated positive impact on human brucellosis prevention (10), currently available vaccines alone cannot eliminate brucellosis in any host species (11). Various control methods are employed, including infected animal culling, herd segregation, and vaccination programs. The prevention, control, and eradication of brucellosis demands substantial financial support, unwavering commitment, and extensive resources (12–13). Successful disease control necessitates implementing mass animal vaccination programs, increasing environmental disinfection frequency, ensuring timely elimination of infected animals, and maintaining persistent disease surveillance systems.

This comprehensive analysis elucidates the disease's transmission trajectory from northern China through the central and developed coastal regions, ultimately reaching the southwestern areas. The synchronized fluctuations in disease incidence between northern and southern regions suggest that effective control measures implemented in the northern could significantly reduce disease prevalence in the southern, though additional evidence is needed to validate this hypothesis. Implementation of integrated surveillance programs incorporating serological, bacteriological, and genomic monitoring in southern regions would provide crucial data to support this relationship. The study demonstrates that brucellosis incidence is intrinsically linked to economic development indicators, including increased mutton, beef, and milk production, as well as rising per capita disposable income, indicating that socioeconomic advancement and growing demand for animal products are primary drivers of persistent brucellosis transmission. Priority should be given to enhancing surveillance and control of infected animals through sustained vaccination programs in high-incidence areas, implementation of systematic

surveillance protocols, and strict regulation of infected animal movement.

Conflicts of interest: No conflicts of interest.

Funding: Supported by the Central Government-Guided Local (Inner Mongolia Autonomous Region) Science and Technology Development Funding Projects (Grant number: 2024ZY0053). The funding agency had no role in study design, data collection and analysis, publication decisions, or manuscript preparation.

doi: 10.46234/ccdcw2025.076

Corresponding authors: Zhenjun Li, lizhenjun@icdc.cn; Canjun Zheng, zhengcj@chinacdc.cn.

¹ National Key Laboratory of Intelligent Tracking and Forecasting for Infectious Diseases, National Institute for Communicable Disease Control and Prevention, Chinese Center for Disease Control and Prevention, Beijing, China; ² Ulanqab Center for Disease Control and Prevention, Jining City, Inner Mongolia Autonomous Region, China; ³ Chinese Center for Disease Control and Prevention, Beijing, China.

Copyright © 2025 by Chinese Center for Disease Control and Prevention. All content is distributed under a Creative Commons Attribution Non Commercial License 4.0 (CC BY-NC).

Submitted: November 29, 2024

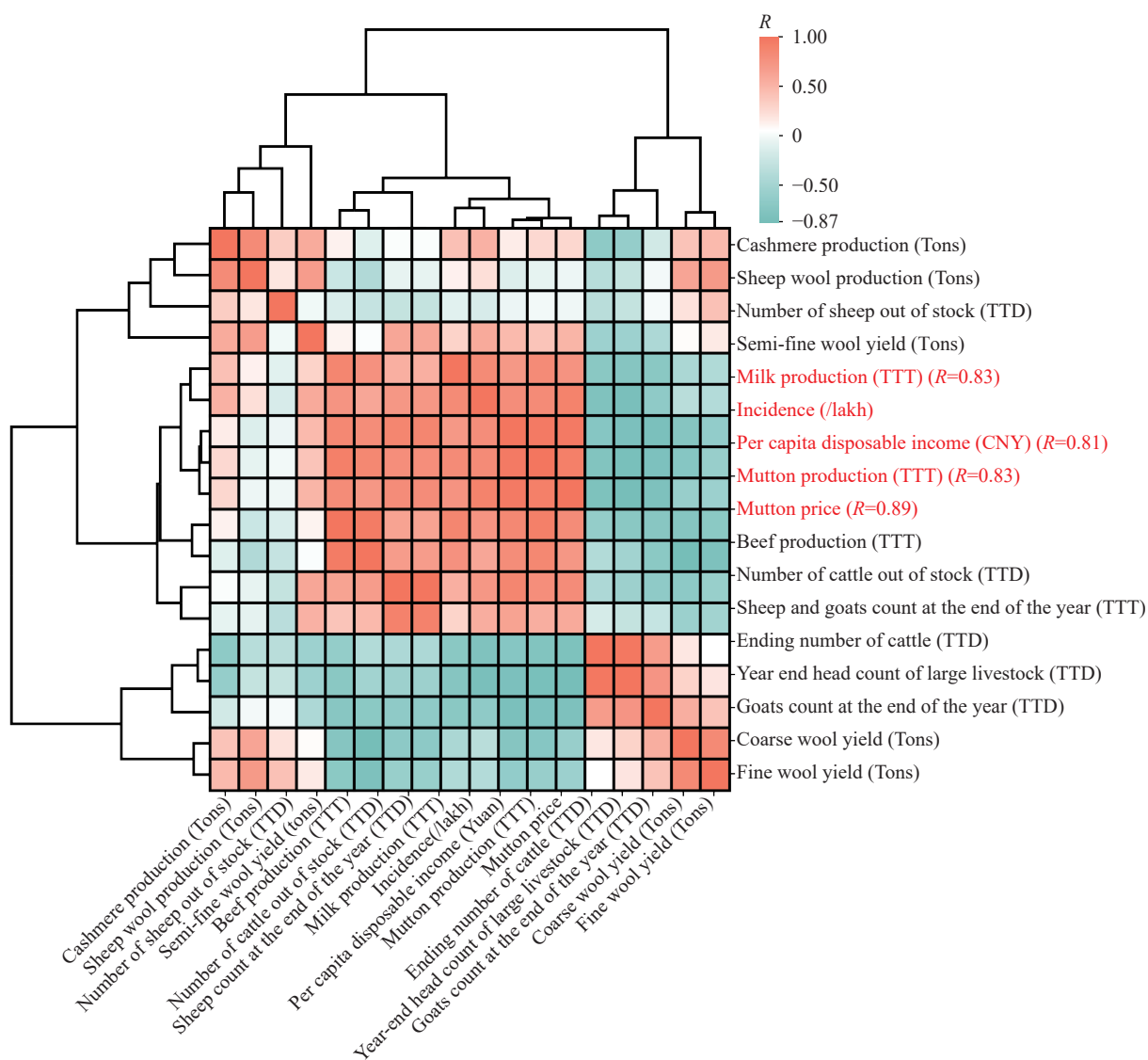
Accepted: March 03, 2025

Issued: April 04, 2025

REFERENCES

- Pisarenko SV, Kovalev DA, Volynkina AS, Ponomarenko DG, Rusanova DV, Zharinova NV, et al. Global evolution and phylogeography of *Brucella melitensis* strains. BMC Genomics 2018;19(1):353. <https://doi.org/10.1186/s12864-018-4762-2>.
- Lai SJ, Zhou H, Xiong WY, Gilbert M, Huang ZJ, Yu JX, et al. Changing epidemiology of human brucellosis, China, 1955-2014. Emerg Infect Dis 2017;23(2):184 – 94. <https://doi.org/10.3201/eid2302.151710>.
- Yang HM, Chen Q, Li Y, Mu D, Zhang YP, Yin WW. Epidemic characteristics, high-risk areas and space-time clusters of human brucellosis - China, 2020-2021. China CDC Wkly 2023;5(1):17 – 22. <https://doi.org/10.46234/ccdcw2023.004>.
- Zhao ZZ. MLVA molecular epidemiological characteristics and in vitro drug susceptibility study of brucella from China [dissertation]. Beijing: The Chinese Center for Disease Control and Prevention; 2017. (In Chinese)
- Yang HX, Zhang SW, Wang TJ, Zhao CH, Zhang XY, Hu J, et al. Epidemiological characteristics and spatiotemporal trend analysis of human brucellosis in China, 1950-2018. Int J Environ Res Public Health 2020;17(7):2382. <https://doi.org/10.3390/ijerph17072382>.
- Darbon A, Valdano E, Poletto C, Giovannini A, Savini L, Candeloro L, et al. Network-based assessment of the vulnerability of Italian regions to bovine brucellosis. Prev Vet Med 2018;158:25 – 34. <https://doi.org/10.1016/j.prevetmed.2018.07.004>.
- Peng C, Li YJ, Huang DS, Guan P. Spatial-temporal distribution of human brucellosis in mainland China from 2004 to 2017 and an analysis of social and environmental factors. Environ Health Prev Med 2020;25(1):1. <https://doi.org/10.1186/s12199-019-0839-z>.
- Cárdenas L, Awada L, Tizzani P, Cáceres P, Casal J. Characterization and evolution of countries affected by bovine brucellosis (1996-2014). Transbound Emerg Dis 2019;66(3):1280 – 90. <https://doi.org/10.1111/tbed.13144>.
- Liang DY, Liu D, Yang M, Wang XM, Li YP, Guo WD, et al. Spatiotemporal distribution of human brucellosis in Inner Mongolia, China, in 2010-2015, and influencing factors. Sci Rep 2021;11(1):24213. <https://doi.org/10.1038/s41598-021-03723-9>.
- Caetano MC, Afonso F, Ribeiro R, Fonseca AP, Abernethy DA, Boinas F. Control of bovine brucellosis from persistently infected holdings using RB51 vaccination with test-and-slaughter: a comparative case report from a high incidence area in Portugal. Transbound Emerg Dis 2016;63(1):e39 – 47. <https://doi.org/10.1111/tbed.12228>.
- Olsen SC, Stoffregen WS. Essential role of vaccines in brucellosis control and eradication programs for livestock. Expert Rev Vaccines 2005;4(6):915 – 28. <https://doi.org/10.1586/14760584.4.6.915>.
- Darbandi A, Koupaei M, Navidifar T, Shahroodian S, Heidary M, Talebi M. Brucellosis control methods with an emphasis on vaccination: a systematic review. Expert Rev Anti Infect Ther 2022;20(7):1025 – 35. <https://doi.org/10.1080/14787210.2022.2066521>.
- Li MT, Sun GQ, Zhang WY, Jin Z. Model-based evaluation of strategies to control brucellosis in China. Int J Environ Res Public Health 2017;14(3):295. <https://doi.org/10.3390/ijerph14030295>.

SUPPLEMENTARY MATERIAL



SUPPLEMENTARY FIGURE S1. Correlation analysis of incidence rate of human brucellosis and animal husbandry factors. Abbreviation: TTD=Ten thousand heads; TTT=Ten thousand tons; CNY=Chinese Yuan.

Preplanned Studies

Epidemic Characteristics of Schistosomiasis — China, 2016–2023

Lijuan Zhang¹; Shizhen Li¹; Jing Xu^{1,2}; Chunli Cao¹; Shizhu Li^{1,2,#}**Summary****What is already known about this topic?**

Schistosomiasis is a water-borne parasitic disease that significantly threatens human health and socioeconomic development. In China, *Schistosoma japonicum* is the predominant pathogenic species, and transmission control criteria were successfully achieved nationwide in 2015.

What is added by this report?

This report comprehensively documents schistosomiasis epidemiology in China from 2016 to 2023, presenting provincial and county-level data on human infections, cattle reservoirs, and *Oncomelania hupensis* snail vector distribution. Serological findings at both provincial and county levels demonstrate persistently elevated seropositive rates in specific regions despite overall progress.

What are the implications for public health practice?

Development of highly sensitive diagnostic tools for low-intensity infections is essential, while intelligent early warning systems and multi-channel surveillance mechanisms must be strengthened to achieve the goal of schistosomiasis elimination in China.

decreased by 49.00%, from 54,454 in 2016 to 27,772 in 2023. The 8-year average seropositive rate across provincial-level administrative divisions (PLADs) was 1.80%, with the highest rates observed in Yunnan (2.99%), Jiangxi (2.84%), and Hunan (2.67%) PLADs. Joinpoint analysis revealed a consistent decline in seropositive rates since 2016 and a significant inflection point was identified in 2021, indicating an acceleration in the rate of decline. No positive cattle have been detected since 2020. The total area of snail habitats exhibited a slight rebound from 356,835 square hectometers (hm²) in 2016 to 367,702 hm² in 2023, with new habitats emerging annually, totaling 4,080 hm² of newly identified habitats.

Conclusions: Development of highly sensitive and specific diagnostic tools is essential, alongside intensified surveillance of wild animal reservoirs and high-risk snail habitats, to achieve the goal of eliminating schistosomiasis by 2030.

ABSTRACT

Introduction: The Chinese government has established targets for elimination of schistosomiasis in all endemic counties by 2028. This study aimed to analyze the epidemiological characteristics of schistosomiasis in China after transmission control and provide a theoretical basis for achieving the county-level elimination goal by 2028.

Methods: Provincial and county-level data on human infection, cattle reservoirs and *Oncomelania hupensis* snail vector distribution were collected from 2016 to 2023, to analyze the trend of schistosomiasis epidemic situation and serological positive rate. Joinpoint regression analysis was employed to analyze seropositive rate trends.

Results: The number of schistosomiasis cases

Schistosomiasis represents a significant and widespread neglected tropical disease (NTD) with substantial public health implications (1). In 2012, the World Health Assembly adopted a resolution targeting the global elimination of schistosomiasis as a public health problem by 2025 (2). China successfully met the criteria for transmission control of schistosomiasis across all provincial-level administrative divisions (PLADs) in 2015. The Healthy China 2030 Plan Outline and the Action Plan for Accelerating the Goal of Schistosomiasis Elimination (2023–2030) have established ambitious targets for transmission interruption and elimination in all endemic counties by 2025 and 2028, respectively (3). To evaluate the challenges associated with progress toward elimination, we analyzed schistosomiasis epidemic data and snail distribution patterns from 2016 to 2023 across 12 PLADs south of the Yangtze River Basin. While our findings demonstrate an overall decline in schistosomiasis prevalence, average seroprevalence remains elevated in certain counties, and snail habitat

areas have rebounded in specific regions. Enhanced surveillance systems and early-warning mechanisms should be developed to facilitate the successful elimination of schistosomiasis in China.

Populations in endemic regions underwent initial screening via serological tests, followed by confirmatory pathogenic examinations for positive cases. Cattle were primarily assessed through pathogenic testing. Snail surveys were systematically conducted across existing, historical, and potential snail habitats. Data from these surveillance activities were collected at both PLAD and county levels from 2016 to 2023 using the National Parasitic Diseases Control Information Management System (NPDCIMS). Seropositive rates were calculated exclusively for counties with a minimum of 100 serological screenings and were stratified into five categories: 0 (no positives), positive rate $\leq 1\%$, $1\% < \text{positive rate} \leq 3\%$, $3\% < \text{positive rate} \leq 5\%$, and positive rate $> 5\%$. Joinpoint regression analysis, a statistical method that identifies significant changes in temporal trends by determining optimal “joining points” that divide time series data into distinct segments, was employed to analyze seropositive rate trends. Snail habitat areas were classified into seven distinct levels to facilitate county-level distribution analysis.

Shanghai Municipality achieved schistosomiasis elimination status in 2015, followed by Guangdong,

Guangxi, Fujian, and Zhejiang PLADs in 2016. Sichuan Province met the transmission interruption criteria in 2017, followed by Jiangsu in 2019, Yunnan and Hubei in 2020, and Hunan, Anhui, and Jiangxi in 2023. Consequently, by 2023, schistosomiasis control across China had successfully achieved the criteria for transmission interruption nationwide.

The number of schistosomiasis cases decreased by 49.00%, from 54,454 in 2016 to 27,772 in 2023, with the proportion of advanced schistosomiasis cases increasing from 56.14% to 99.99%. During this period, only 3 acute schistosomiasis cases were reported: one from Jiangxi in 2019 and 2 domestic imported cases from other PLADs. Table 1 presents the serological and parasitological test results for schistosomiasis in human and cattle hosts stratified by PLAD. In total, 3,134,928 person-times underwent parasitological testing, with 636 positive results. The 8-year average seropositive rate across PLADs was 1.80%, with the highest rates observed in Yunnan (2.99%), Jiangxi (2.84%), and Hunan (2.67%) PLADs. Based on transmission status by the end of 2023, with 354 counties at the elimination stage and 97 counties at the transmission interruption stage, the seropositive rates for elimination and transmission interruption groups were 0.70% and 1.43%, respectively.

Joinpoint analysis revealed a consistent decline in seropositive rates since 2016 (Figure 1A). A significant

TABLE 1. Serological screening and stool examination results for humans and cattle across 12 PLADs with schistosomiasis endemicity in China, 2016–2023.

PLADs	Serological and stool test in humans					Stool test in cattle	
	Number of serological tests	Number of seropositive cases	Seroprevalence (%)	Number of stool examinations	Number of egg-positives	Number of stool examinations	Number of egg-positives
Anhui	8,424,835	87,147	1.03	752,981	1	111,079	0
Fujian	30,346	3	0.01	1	0	3,280	0
Guangdong	29,474	32	0.11	34	0	0	0
Guangxi	48,920	47	0.10	17,068	0	31,747	0
Hubei	8,986,835	155,445	1.73	291,749	1	117,149	0
Hunan	7,725,475	206,097	2.67	267,708	582	288,684	3
Jiangsu	2,987,651	18,132	0.61	326,455	2	1,340	0
Jiangxi	4,570,976	129,910	2.84	333,270	21	115,244	15
Shanghai	180,006	203	0.11	161	2	0	0
Sichuan	11,165,107	187,858	1.68	870,261	0	26,806	0
Yunnan	1,880,313	56,243	2.99	271,450	0	465,474	0
Zhejiang	817,946	3,596	0.44	3,790	27	3,968	0
Total	46,847,884	844,713	1.80	3,134,928	636	1,164,771	18

Abbreviation: PLAD=provincial-level administrative division.

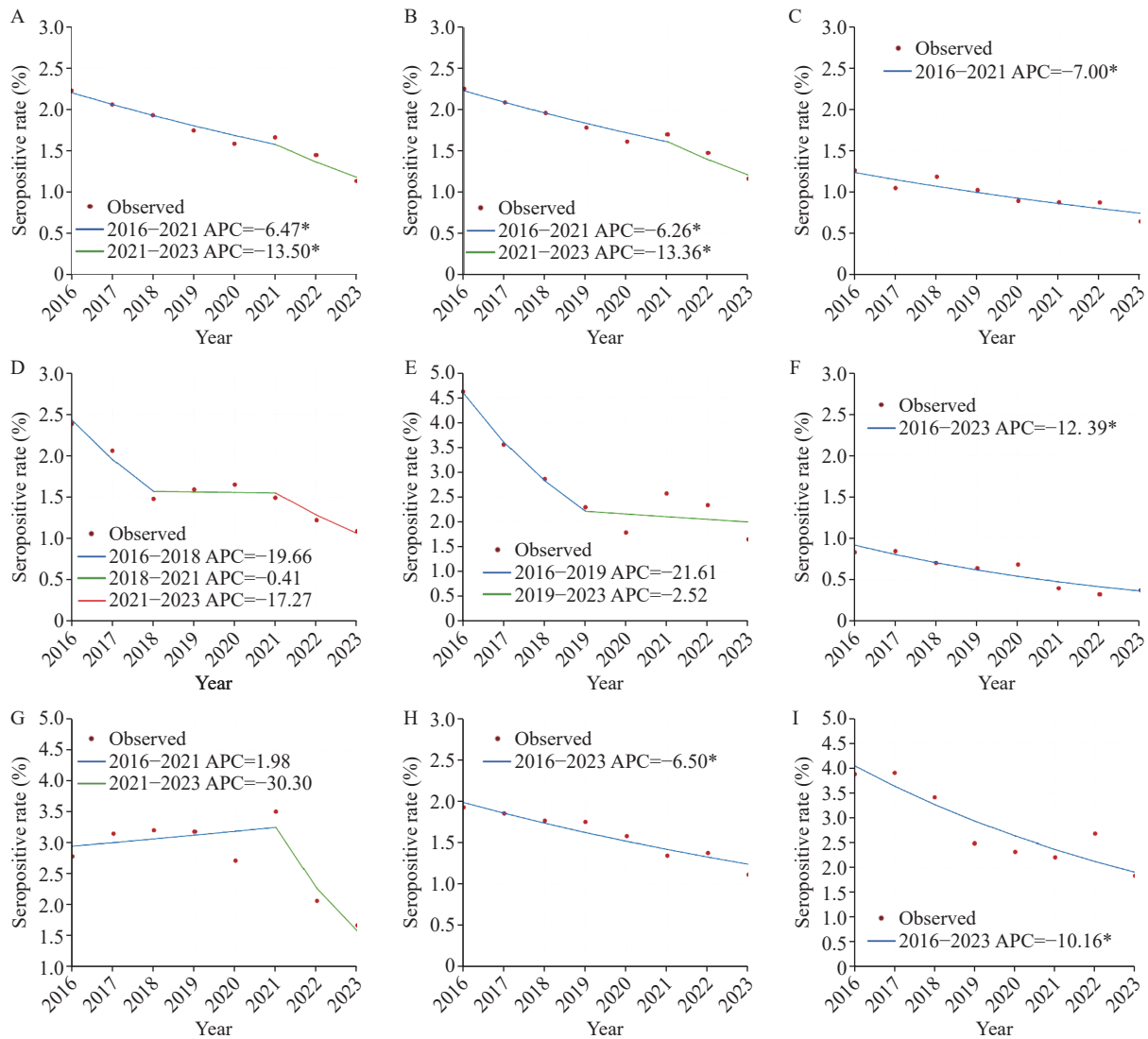


FIGURE 1. Jointpoint regression analysis of schistosomiasis seroprevalence trends from 2016 to 2023 across endemic regions in China. (A) One jointpoint for the 12 endemic PLADs. (B) One jointpoint for the 7 endemic PLADs. (C) Zero jointpoint for Anhui Province. (D) Two jointpoints for Hubei Province. (E) One jointpoint for Hunan Province. (F) Zero jointpoint for Jiangsu Province. (G) One jointpoint for Jiangxi Province. (H) Zero jointpoint for Sichuan Province. (I) Zero jointpoint for Yunnan Province.

Abbreviation: PLADs=provincial-level administrative divisions; APC=annual percent change.

inflection point was identified in 2021, indicating an acceleration in the rate of decline. Across the 12 endemic PLADs, the annual percent change (APC) shifted from -6.47% to -13.50% , while for the 7 PLADs where schistosomiasis has not been eliminated, the APC shifted from -6.26% to -13.36% (Figure 1A, B). At the provincial level, Anhui, Jiangsu, Sichuan, and Yunnan demonstrated continuous downward trends without significant turning points, with APCs ranging from -6.5% to -12.39% , indicating steady and consistent declines throughout the study period (Figure 1C, 1F, 1H, 1I). However, Hunan exhibited a

distinct pattern with a turning point in 2019, after which the rate of decline plateaued substantially, with the APC shifting from -21.61% to -2.52% (Figure 1E). In contrast, Jiangxi demonstrated a brief upward trend prior to a turning point in 2021, followed by a precipitous decline thereafter (APC: 1.98% , -30.3% , Figure 1G). Hubei presented a more complex pattern with two turning points identified in 2018 and 2021, characterized by a relatively stable trend between 2018 and 2021 (APC: -19.66% , -0.41% , -17.27% , Figure 1D).

Figure 2A illustrates the distribution of counties

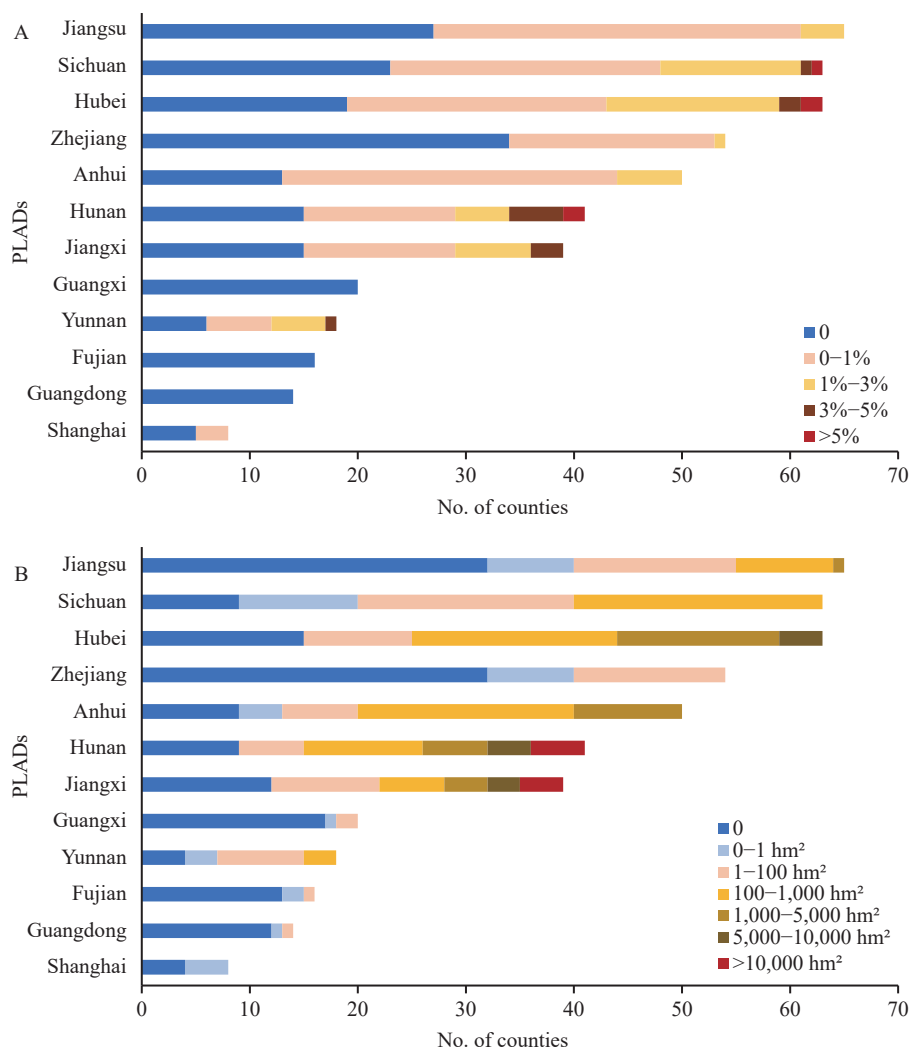


FIGURE 2. Number of counties with different levels of seropositive rates and snail habitat areas in 12 PLADs with schistosomiasis endemic regions in China, 2023. (A) Seropositive rates of schistosomiasis; (B) Snail habitat areas. Abbreviation: PLADs=provincial-level administrative divisions.

with varying seroprevalence levels across PLADs in 2023. Among all 451 counties, 207 reported zero seropositive cases, while 170 had seropositive rates between 0–1%, 57 between 1%–3%, 12 between 3%–5%, and 5 counties exceeded 5%. The 12 counties with seropositive rates between 3%–5% were distributed across Hunan ($n=5$), Jiangxi ($n=3$), Hubei ($n=2$), Sichuan ($n=1$), and Yunnan ($n=1$). The 5 counties with seropositive rates exceeding 5% were located in Hunan ($n=2$), Hubei ($n=2$), and Sichuan ($n=1$).

The population of cattle hosts in endemic villages decreased by 38.76%, from 881,050 in 2016 to 539,548 in 2023. During this period, a comprehensive surveillance program examined 1,164,771 herd-time cattle through stool examinations, identifying only 18 positive cases, all reported from Jiangxi and Hunan

Provinces (Table 1). Notably, no positive cattle have been detected since 2020.

The total area of snail habitats exhibited a slight rebound from 356,835 square hectometers (hm^2) in 2016 to 367,702 hm^2 in 2023, with new habitats emerging annually, totaling 4,080 hm^2 of newly identified habitats. From 2016 to 2019 and 2021 to 2023, no infected snail habitats were detected across any schistosomiasis-endemic region; however, in 2020, 1.96 hm^2 of habitats containing infected snails were identified in Anhui Province. Figure 2B illustrates the distribution of counties with varying levels of snail habitat areas across all 12 PLADs in 2023. Among the 451 counties surveyed, the number of counties with snail habitat areas of 0, 0–1, 1–100, 100–1000, 1,000–5,000, 5,000–10,000, and $\geq 10,000$ hm^2 were 168, 42, 94, 91, 36, 11, and 9, respectively. The 11

counties with snail habitat areas of 5,000–10,000 hm² were distributed across Hunan ($n=4$), Hubei ($n=4$), and Jiangxi ($n=3$). The 9 counties with snail habitat areas $\geq 10,000$ hm² were concentrated in Hunan ($n=5$) and Jiangxi ($n=4$).

DISCUSSION

Data from 2016 to 2023 indicate a substantial decline in schistosomiasis prevalence across China. Infection rates in both human and cattle populations decreased significantly, with no infected snails detected for several consecutive years, except for a single environment containing infectious snails identified in 2020. Joinpoint analysis revealed a consistent downward trend in serological positivity rates; however, certain counties still reported seroprevalence exceeding 5% in 2023. These five counties with elevated seroprevalence predominantly represent historical high-risk areas for schistosomiasis transmission. Positive serological results reflect cumulative infection exposure over time, with higher positivity rates among specific populations indicating increased exposure risk and suggesting potential ongoing transmission in counties with elevated rates (4). The true epidemic situation may be underestimated in low-prevalence settings due to limitations in detection technology or misdiagnosis (5).

Snail habitat areas exhibited a slight rebound during 2016–2023, with new habitats identified annually, particularly following the 2020 flood disaster along the Yangtze River Basin (6). Flood events, rice seedling transplantation, and wetland construction all presented significant challenges for snail control during this period. The livestock sector reported only 18 cattle testing positive since 2016, suggesting that comprehensive prevention and control strategies — particularly those targeting infectious sources such as buffaloes — have effectively controlled bovine infection. However, *Schistosoma japonicum* can infect over 40 mammalian species, including cattle, sheep, dogs, other domestic animals, as well as rodents and various wildlife species (7). The increasing population density of wild animals has amplified their role in schistosomiasis transmission dynamics (8).

It is important to note that serological tests cannot differentiate between current and historical infections. In regions with low endemic prevalence, research efforts should focus on developing advanced molecular diagnostic methods for schistosomiasis to minimize false negatives and enable precision-targeted prevention

and control strategies (9). Additionally, comprehensive surveillance should be implemented for both domestic and wild animal reservoirs in high-risk transmission areas to facilitate robust monitoring and early warning systems.

A key limitation of this study was the absence of data regarding specific schistosomiasis control interventions, which would have been valuable for evaluating the effectiveness of particular strategies. Furthermore, detailed information on serologically positive cases, including antibody titers and historical infection status, was not collected for comprehensive analysis. Consequently, this investigation primarily focused on reporting epidemiological trends rather than intervention outcomes.

In conclusion, schistosomiasis in China has reached a low endemic level, with the majority of cases now classified as advanced disease. Cattle infections in endemic regions have been successfully reduced to zero over the past four years. However, positive cattle fecal samples detected during rapid risk assessments in 2019 and 2021 (10) reveal persistent transmission risks in certain areas. The recently issued Action Plan for Accelerating the Goal of Schistosomiasis Elimination (2023–2030) outlines six strategic initiatives to advance elimination efforts. To achieve the goal of eliminating schistosomiasis across all endemic counties by 2030, development of highly sensitive and specific diagnostic tools is essential, alongside intensified surveillance of wild animal reservoirs and high-risk snail habitats.

Conflicts of interest: No conflicts of interest.

Acknowledgements: All participants involved in schistosomiasis examination, snail surveillance, and data collection activities.

Funding: Supported by the Three-Year Initiative Plan for Strengthening Public Health System Construction in Shanghai (2023–2025) Key Discipline Project (GWVI-11.1-12).

doi: 10.46234/ccdcw2025.077

Corresponding author: Shizhu Li, lisz@chinacdc.cn.

¹ National Key Laboratory of Intelligent Tracking and Forecasting for Infectious Diseases, Key Laboratory on Parasite and Vector Biology, Ministry of Health, WHO Centre for Tropical Diseases; National Center for International Research on Tropical Diseases, Ministry of Science and Technology, National Institute of Parasitic Diseases, Chinese Center for Disease Control and Prevention (Chinese Center for Tropical Diseases Research), Shanghai, China; ² School of Global Health, Chinese Center for Tropical Diseases Research-Shanghai Jiao Tong University School of Medicine, Shanghai, China.

Copyright © 2025 by Chinese Center for Disease Control and Prevention. All content is distributed under a Creative Commons Attribution Non Commercial License 4.0 (CC BY-NC).

Submitted: December 18, 2024

Accepted: March 13, 2025

Issued: April 04, 2025

REFERENCES

1. Maier T, Wheeler NJ, Namigai EKO, Tycko J, Grewelle RE, Woldeamanuel Y, et al. Gene drives for schistosomiasis transmission control. *PLoS Negl Trop Dis* 2019;13(12):e0007833. <https://doi.org/10.1371/journal.pntd.0007833>.
2. Wiegand RE, Fleming FM, de Vlas SJ, Odiere MR, Kinung'hi S, King CH, et al. Defining elimination as a public health problem for schistosomiasis control programmes: beyond prevalence of heavy-intensity infections. *Lancet Glob Health* 2022;10(9):e1355 – 9. [https://doi.org/10.1016/S2214-109X\(22\)00287-X](https://doi.org/10.1016/S2214-109X(22)00287-X).
3. Wang Q, Xu J, Xia ZG, Han S, Zhang Y, Qian MB, et al. Epidemic status and key tasks for the control and elimination of key parasitic diseases in China. *Chin J Parasitol Parasit Dis* 2024;42(1):1 – 7. <https://doi.org/10.12140/j.issn.1000-7423.2024.01.001>.
4. Xie SY, Yuan M, Ji MJ, Hu F, Li ZJ, Liu YM, et al. Immune responses result in misdiagnosis of *Schistosoma japonicum* by immunodiagnosis kits in egg-positive patients living in a low schistosomiasis transmission area of China. *Parasit Vectors* 2014;7:95. <https://doi.org/10.1186/1756-3305-7-95>.
5. King CH, Galvani AP. Underestimation of the global burden of schistosomiasis. *Lancet* 2018;391(10118):307 – 8. [https://doi.org/10.1016/S0140-6736\(18\)30098-9](https://doi.org/10.1016/S0140-6736(18)30098-9).
6. Xue JB, Wang XY, Zhang LJ, Hao YW, Chen Z, Lin DD, et al. Potential impact of flooding on schistosomiasis in Poyang Lake regions based on multi-source remote sensing images. *Parasit Vectors* 2021;14(1):116. <https://doi.org/10.1186/s13071-021-04576-x>.
7. Lin JJ. Endemic status and control of animal schistosomiasis in China. *Chin J Schisto Control* 2019;31(1):40 – 6. <https://doi.org/10.16250/j.32.1374.2018313>.
8. Lü SB, Chen NG, Liu YM, Zhou LY, Wang YS, Hu F, et al. Survey of *Schistosoma japonicum* infections in wild animals in hilly transmission-controlled areas of Jiangxi Province. *Chin J Schisto Control* 2019; 31(5):463 – 7. <https://doi.org/10.16250/j.32.1374.2019040>.
9. He P, Gordon CA, Williams GM, Li YS, Wang YY, Hu JJ, et al. Real-time PCR diagnosis of *Schistosoma japonicum* in low transmission areas of China. *Infect Dis Poverty* 2018;7(1):8. <https://doi.org/10.1186/s40249-018-0390-y>.
10. He JY, Zhu HQ, Bao ZP, Zhang LJ, Li YL, Feng T, et al. Rapid assessment on potential risks of Schistosomiasis transmission — 7 PLADs, China, 2019 and 2021. *China CDC Wkly* 2021;3(51):1089 – 92. <https://doi.org/10.46234/ccdcw2021.263>.

Methods and Applications

A Novel Matching Pursuit Modeling Strategy Based on Adaptive Fourier Decomposition Theory for Predicting Antigenic Variation of Influenza A (H1N1)

Wei Qu^{1,2,&}; Ruihan Chen^{3,&}; Yang Wang^{1,3,4}; Zhiqi Zeng^{5,6,7}; Cheng Gao⁸; Weiqi Pan^{1,9};
Tao Qian^{10,#}; Chitin Hon^{3,9,#}; Zifeng Yang^{1,4,#}

ABSTRACT

Introduction: Seasonal influenza poses a significant public health burden, causing substantial morbidity and mortality worldwide each year. In this context, timely and accurate vaccine strain selection is critical to mitigating the impact of influenza outbreaks. This article aims to develop an adaptive, universal, and convenient method for predicting antigenic variation in influenza A(H1N1), thereby providing a scientific basis to enhance the biannual influenza vaccine selection process.

Methods: The study integrates adaptive Fourier decomposition (AFD) theory with multiple techniques — including matching pursuit, the maximum selection principle, and bootstrapping — to investigate the complex nonlinear interactions between amino acid substitutions in hemagglutinin (HA) proteins (the primary antigenic protein of influenza virus) and their impact on antigenic changes.

Results: Through comparative analysis with classical methods such as Lasso, Ridge, and random forest, we demonstrate that the AFD-type method offers superior accuracy and computational efficiency in identifying antigenic change-associated amino acid substitutions, thus eliminating the need for time-consuming and expensive experimental procedures.

Conclusion: In summary, AFD-based methods represent effective mathematical models for predicting antigenic variations based on HA sequences and serological data, functioning as ensemble algorithms with guaranteed convergence. Following the sequence of indicators specified in I , we perform a series of operations on A_1 , including feature extension, extraction, and rearrangement, to generate a new input dataset A_1 for the prediction step. With this newly prepared input, we can compute the predicted results as $A_1 W$.

Seasonal influenza remains a significant global public health threat, with the World Health Organization (WHO) estimating 3 to 5 million severe cases and 290,000 to 650,000 deaths annually (1). The predominant circulating strains — influenza A virus subtype H1N1 [A(H1N1)], A(H3N2), and B(Victoria) — undergo antigenic drift due to amino acid substitutions in the hemagglutinin (HA) protein. These molecular changes enable the virus to evade host immunity, resulting in seasonal outbreaks (2–3). Traditional serologic assays, such as hemagglutination inhibition (HI), are employed to monitor antigenic changes but are labor-intensive, costly, and require live virus isolation (4). Consequently, a sequence-based strategy to predict antigenic variants would represent a more efficient alternative (5).

Several machine learning models have been developed for HA sequence-based antigenicity prediction, including support vector machines (SVM), multi-task learning sparse group lasso (MTL-SGL), iterative filtering models, and ridge regression. These approaches demonstrate robust performance in high-dimensional data classification, integrating multiple features with numerical weighting (6–8). However, these models exhibit limitations in handling dynamic data and nonlinear relationships, rendering predictions susceptible to noise, missing values, and feature correlation.

In this article, we introduce a matching pursuit model based on adaptive Fourier decomposition (AFD) theory for predicting influenza antigenic variation, using H1N1 as an exemplar. Inspired by (9) and (10), our model offers three distinct advantages: Adaptivity and efficiency via an AFD maximum selection that mitigates overfitting on small datasets; Nonlinearity and interpretability through capturing epistatic effects between amino acid changes and spatial positions; Robustness via feature screening,

bootstrapping, and orthogonal projection for dual-site interactions.

METHODS

Matching Pursuit Model Based on Adaptive Fourier Decomposition Theory

This section develops a quantitative model to predict antigenic distances from HA protein sequences. We denote A as the independent features and Y as the target variable. Details on the matching pursuit model and prediction procedure are provided in the Supplementary Material (available at <https://weekly.chinacdc.cn/>).

In this section, we outline the specific steps of the model algorithm, which are divided into two main phases: training and predicting, which are shown in Table 1 and Table 2, respectively.

Assuming the execution of the above algorithm stops at step $j = p_\epsilon (\leq p)$, and we obtain the parameter set $X = (x_1, \dots, a_{I_{p_\epsilon}})$ for the training model and the index set $I = (I_1, \dots, I_{p_\epsilon})$. Let $B = (b_1, \dots, b_{p_\epsilon})$ represent the orthonormal matrix, and $A = (a_{I_1}, \dots, a_{I_{p_\epsilon}})$ represent the rearranged matrix of A according to I . We can compute $W_{p_\epsilon \times p_\epsilon}$ using $B = A W$, which gives us the parameter set $W = W X^T$ for prediction model. The subsequent algorithm will help us derive the parameter set for the prediction model and present the prediction results.

Both algorithms generate sequence data through feature expansion, which can lead to a high-dimensional space and increased overfitting risk — especially when higher-order terms are included. However, our model mitigates this via a maximum selection principle and by applying expansion to both training and testing sets. To balance enhanced

TABLE 1. Matching pursuit algorithm — training model.

Step	Process
Input	sequence data $A_{q \times p} = (a_1, \dots, a_q)$ and antigenic data $Y_{q \times 1}$
Output	the parameter set X , the index set I and the result $\tilde{Y}_{q \times 1}$
0	Initialize $\epsilon > 0$, $j = 1$ $b_k \leftarrow a_k / \ a_k\ $, $k = 1, \dots, p$ $I_1 \leftarrow \operatorname{argmax}_k \langle Y, b_k \rangle ^2$ $b_1 \leftarrow a_{I_1} / \ a_{I_1}\ $ $x_1 \leftarrow \langle Y, b_1 \rangle$ $\tilde{Y} \leftarrow \langle Y, b_1 \rangle b_1$ energy $\leftarrow x_1 ^2$
1	While energy $\geq \epsilon$ && $j < p$ do
2	$j \leftarrow j + 1$
3	$b_k \leftarrow Q_{\delta_{j-1}}(b_k) / \ Q_{\delta_{j-1}}(b_k)\ $, $k = 1, \dots, p$
4	$I_j \leftarrow \operatorname{argmax}_k \langle Y, b_k \rangle ^2$
5	$b_j \leftarrow b_{I_j}$
6	$x_j \leftarrow \langle Y, b_j \rangle$
7	$\tilde{Y} \leftarrow \tilde{Y} + \langle Y, b_j \rangle b_j$
8	energy $\leftarrow x_j ^2$
9	End while

TABLE 2. Matching pursuit algorithm — predicting model.

Step	Process
Input	X , I , W , and new sequence data, denoted by $A_{q_1 \times p}$
Output	prediction result, denoted by $\tilde{Y}_{q_1 \times 1}$
0	extract and rearrange a subset of $A_{q_1 \times p}$ according to I ; then obtain \tilde{A}_1 with size $q_1 \times p_\epsilon$
1	compute $W = W A^T$
2	compute $\tilde{Y}_{q_1 \times 1} = \tilde{A}_1 W$

prediction accuracy with the increased computational cost of higher dimensions, we randomly select a small subset of features, choose an appropriate expansion degree (e.g., 2nd or 3rd), and then perform random feature sampling with replacement. The final prediction is obtained by averaging across all iterations, leveraging ensemble methods similar to those used in random forests.

Validation Examples

The dataset description is provided in the Supplementary Materials. In this section, we first present the model's training and prediction results, followed by an evaluation using multiple performance metrics. We then discuss the reliability of key sites identified by the model, particularly in the context of antigenic variation. We employ two primary evaluation metrics to assess model effectiveness: root mean square error (RMSE) and F1-score, defined as follows.

$$RMSE = \sqrt{\frac{1}{n} \sum_{i=1}^n (Y_i - \tilde{Y}_i)^2}$$

where Y represents the true value and \tilde{Y} represents the predicted result

For each analytical task, we employ Algorithm 1 for training and Algorithm 2 for prediction. We benchmark our approach against five classical methods: Random Forest (RF), Support Vector Regression (SVR), Lasso, Gradient Boosting (GB), and Elastic Net (EN). Our proposed model is Matching Pursuit Method (MP).

RESULTS

Model Evaluation

We established epsilon values of 0.1, 0.01, 0.01,

0.001, and 0.01, with bootstrap samples of 30, 5, 5, 2, and 15 across the five tasks, respectively. Each task incorporated 70, 80, 70, 80, and 80 observations drawn with replacement from the original dataset. Subsequently, we calculated the mean for each of these samples. From a theoretical perspective, as the number of selected observations decreases, the number of bootstrap samples should increase proportionally. The evaluation metrics for the training model are presented in Table 3.

The five tasks above demonstrate that our method performs robustly across these datasets. The approach proves effective both in capturing positive events, such as site variations, and in optimizing the balance between accuracy and recall rate.

Figure 1 displays the MP model's training results for antigenic distance prediction, where blue dots closer to the red line indicate superior performance. We subsequently applied Kernel Density Estimation (KDE) with a bandwidth of 0.5 to generate smooth density curves for both predicted and actual data. The substantial overlap between these curves reveals similar distributions and minimal bias. As illustrated in Figure 2, this alignment across datasets confirms the model's strong generalization capabilities, consistency, and robustness.

The evaluation metrics for the prediction model are presented in Table 4.

The prediction results across the five tasks above reveal that, while our model demonstrates strong performance during training, the prediction outcomes still present opportunities for improvement. Despite systematic efforts to optimize parameters and refine the input dataset during model development, certain aspects remain suboptimal. Nevertheless, these numerical results provide valuable reference points for subsequent research endeavors.

TABLE 3. Comparison of training performance between classical models and AFD-based predictive methods on five H1N1 prediction tasks.

Methods	Task 1		Task 2		Task 3		Task 4		Task 5	
	RMSE	F1-score								
RF	0.624	0.730	0.380	0.899	0.453	0.909	0.326	0.984	0.366	0.816
SVR	0.203	0.955	0.343	0.956	0.506	0.890	0.323	0.968	0.335	0.883
Lasso	1.317	0.543	1.322	0.867	1.635	0.113	0.905	0.878	1.340	0.520
GBR	0.763	0.730	0.708	0.867	0.790	0.808	0.561	0.878	0.433	0.768
ENG	0.519	0.909	0.597	0.932	0.627	0.863	0.371	0.984	0.341	0.816
MP	0.149	0.978	0.296	0.963	0.312	0.939	0.195	1.000	0.261	0.930

Note: The bolded values highlight the best performance scores across different models for each H1N1 prediction task.

Abbreviation: RF=random forest; SVR=support vector regression; GBR=gradient boosting regression; ENG=elastic net; MP=matching pursuit method; RMSE=root mean square error.

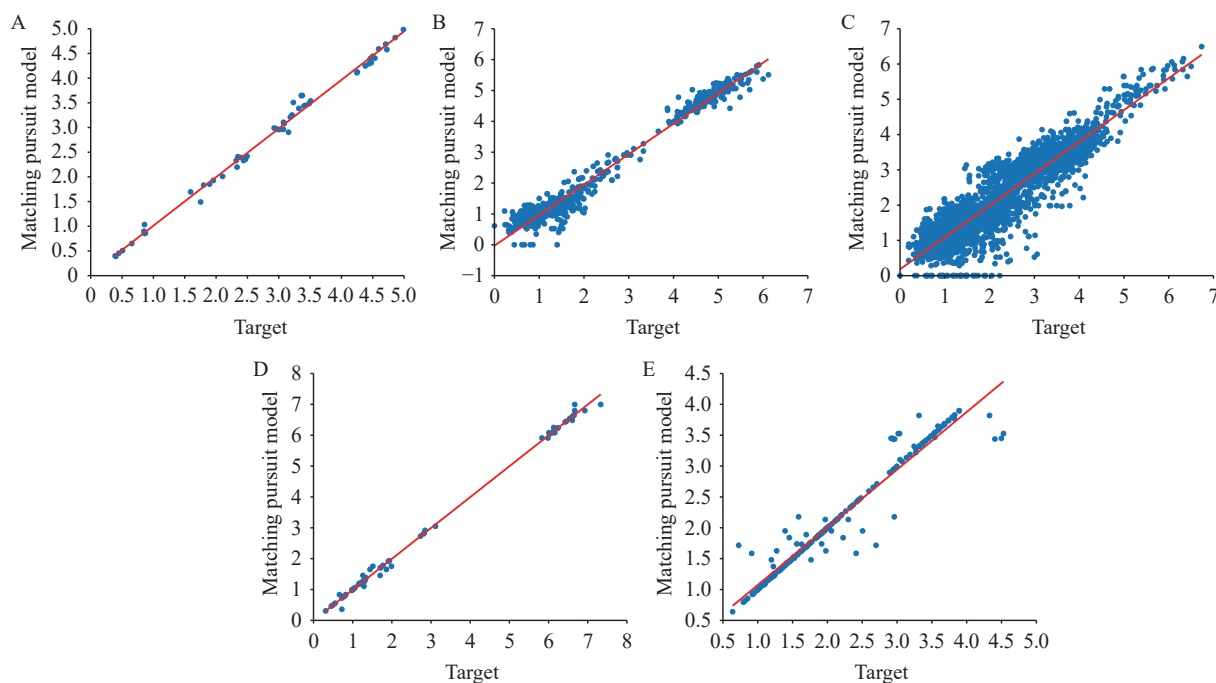


FIGURE 1. Training results of the MP model for antigenic distance prediction across (A–E) Tasks 1–5. Note: The X-axis represents the ground truth antigenic distance, and the Y-axis shows the predicted values. The red diagonal line is the correlation line. Abbreviation: MP=matching pursuit method.

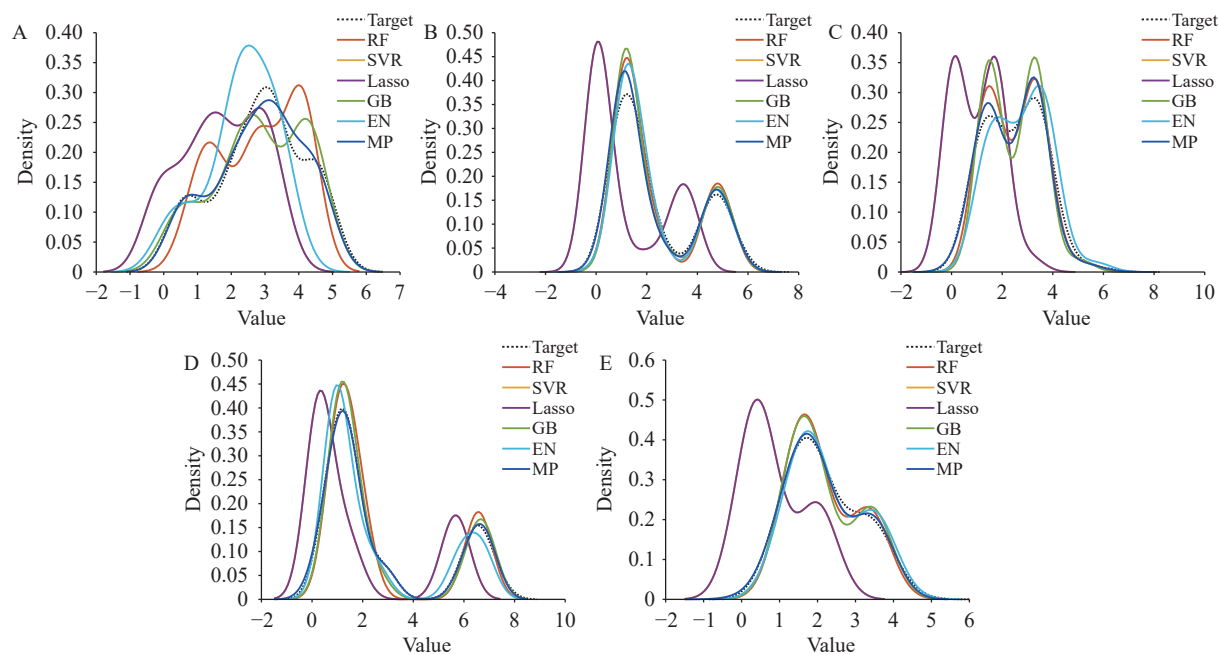


FIGURE 2. Training results of the classical and MP model represented through Kernel Density Estimation (KDE) distributions of predicted and actual antigenic distance values across (A–E) Task 1–5. Note: The X-axis denotes the antigenic distance, and the Y-axis indicates the density. Each line corresponds to a different model. Abbreviation: MP=matching pursuit method.

Figure 3 illustrates the prediction results for antigenic distance using the MP model. The proximity of blue dots to the red line indicates prediction

accuracy. Figure 4 displays the KDE results for all six methods, demonstrating that our approach yields superior testing outcomes. The degree of overlap with

the target curve directly corresponds to prediction performance quality.

Analysis on Amino Acid Site

In this section, we conducted a systematic screening and evaluation of critical amino acid sites within the model. The top 50 amino acid sites with the highest contribution were selected for model fitting in each task. Task 1 comprised 8 single sites and 34 coupled sites, task 2 included 13 single sites and 37 coupled sites, task 3 contained 12 single sites and 38 coupled sites, task 4 had 8 single sites and 32 coupled sites, and

task 5 consisted of 7 single sites and 43 coupled sites. Notably, coupled sites consistently represented a higher proportion in feature selection across all tasks, ranging from 74–86 percent (Table 5 and Table 6).

We identified 21, 29, 39, 37, and 53 amino acid mutations in tasks 1–5, with 16, 20, 29, 22, and 28 sites respectively associated with antigenic epitopes (Table 7 and Figure 5). These findings suggest that mutations at these positions may significantly alter antigenicity and contribute to antigenic drift. Notably, certain amino acid positions appeared repeatedly in coupled-site mutations, such as positions 216 and 186

TABLE 4. Comparison of predicting performance between classical models and AFD-based predictive methods on five H1N1 prediction tasks.

Methods	Task 1		Task 2		Task 3		Task 4		Task 5	
	RMSE	F1-score								
RF	0.678	0.942	0.573	0.891	0.523	0.905	0.405	0.941	0.556	0.817
SVR	1.065	0.821	0.757	0.913	0.570	0.889	0.799	0.898	0.526	0.871
Lasso	1.315	0.517	1.301	0.891	1.617	0.111	1.334	0.806	1.414	0.164
GBR	0.942	0.826	0.747	0.891	0.786	0.827	1.582	0.570	0.661	0.796
ENG	0.653	0.921	0.780	0.927	0.610	0.877	0.456	0.962	0.546	0.844
MP	0.582	0.942	0.478	0.944	0.513	0.914	0.403	0.941	0.416	0.915

Note: The bolded values highlight the best performance scores across different models for each H1N1 prediction task.

Abbreviation: RF=random forest; SVR=support vector regression; GBR=gradient boosting regression; ENG=elastic net; MP=matching pursuit method; RMSE=root mean square error.

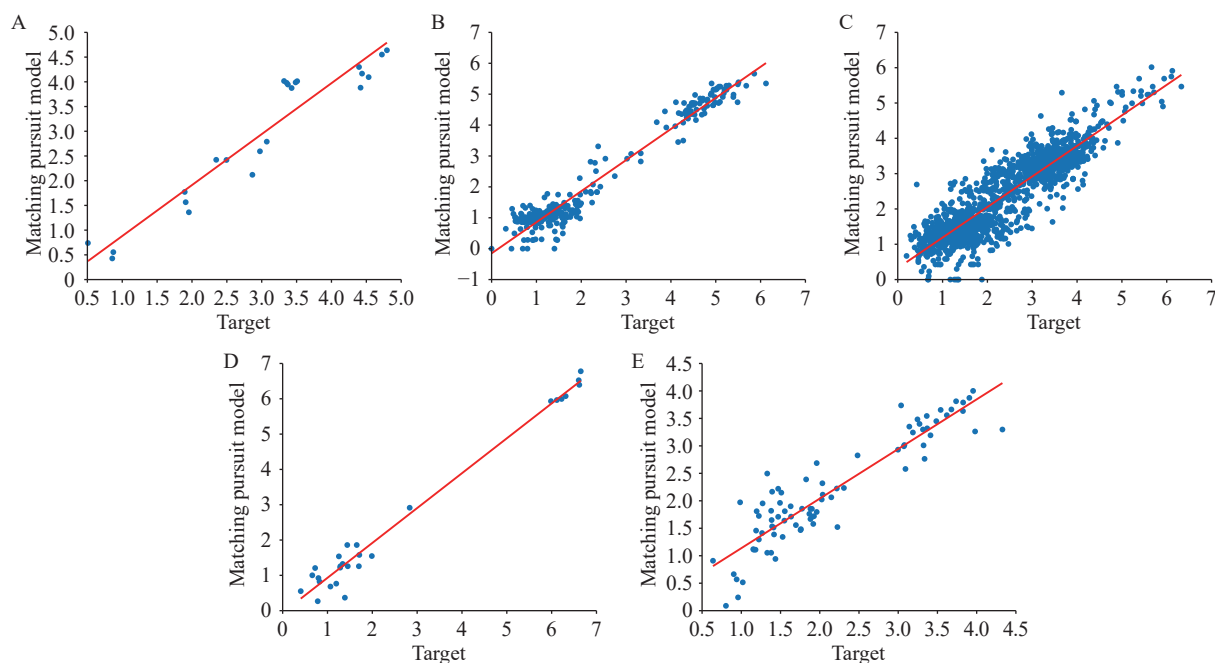


FIGURE 3. Predicting results of the MP model for antigenic distance prediction across (A–E) Task 1–5.

Note: The X-axis represents the ground truth antigenic distance, and the Y-axis shows the predicted values. The red diagonal line is the correlation line.

Abbreviation: MP=matching pursuit method.

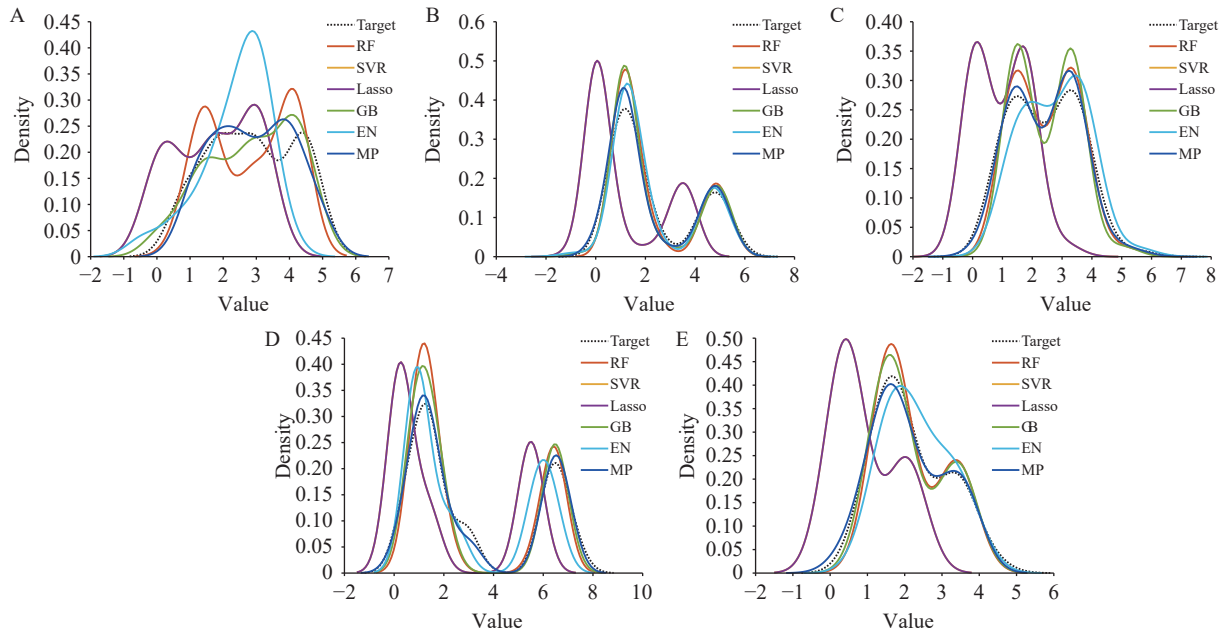


FIGURE 4. Predicting results of the classical and MP model represented through KDE distributions of predicted and actual antigenic distance values across (A–E) Task 1–5.

Note: The X-axis denotes the antigenic distance, and the Y-axis indicates the density. Each line corresponds to a different model.

Abbreviation: KDE=kernel density estimation; MP=matching pursuit method.

TABLE 5. Top single amino acid sites identified for their high contribution to antigenic changes within each task based on the MP model (Single Site).

Task 1 (8)	Task 2 (13)	Task 3 (12)	Task 4 (8)	Task 5 (7)
54	43	43	51	9
56	66	57	120	34
71	74	82	155	49
121	84	132	186	77
128	89	141	211	81
135	125	186	216	93
186	141	187	260	95
187	153	189	272	
	163	190		
	187	222		
	215	252		
	222	315		
	253			

Note: The number after Task No. is the important feature number. Abbreviation: MP=matching pursuit method.

in task 1, 253 in task 2, 187 and 141 in task 3, 211 in task 4, and 209 and 35 in task 5. The recurrence of these mutations in both single-site and coupled-site analyses indicates their substantial impact on antigenic properties (Table 6 and Figure 6).

Based on the results shown in Table 6 and Figure 5,

we have identified both commonalities and differences across individual tasks. Certain amino acid sites consistently appear in multiple tasks, such as the 153 site in the Sa region, which is identified as critical in almost all tasks, suggesting its central role in antigenic variation. Conversely, some loci appear exclusively in specific tasks, reflecting the diversity of antigenic variations that may be influenced by different datasets or model conditions.

Finally, we summarized and deduplicated the amino acids in six antigenic epitopes (Ca, Cb, Pa, Pb, Sa, and Sb) selected from the five tasks. A total of 12 residues are present in the Ca antigenic epitope, 13 in the Cb antigenic epitope, 8 in the Pa antigenic epitope, 4 in the Pb antigenic epitope, 11 in the Sa antigenic epitope, and 12 in the Sb antigenic epitope. All residues were visualized on both trimeric and monomeric structures of the influenza HA protein (PDB: 3UBE) using PyMOL (Figure 7).

The identification of these key sites provides valuable insights for elucidating antigenic variation mechanisms and serves as a critical reference for vaccine design. Specifically, optimizing vaccine formulations to target these frequently occurring critical sites could substantially enhance vaccine efficacy against emerging viral strains.

TABLE 6. Top coupled amino acid sites identified for their high contribution to antigenic changes within each task based on the MP model.

Task No.	Two Site									
Task 1 (34)	187–222	135–186	121–216	56–253	186–216	71–130	71–186	193–216	54–272	121–187
	56–193	54–56	56–216	36–186	153–160	128–186	128–193	193–253	74–141	36–193
	141–157	135–141	186–253	128–253	71–135	74–135	160–324	36–157	36–216	56–130
	135–160	160–216	157–272	135–222						
Task 2 (37)	69–125	187–253	153–187	43–125	153–253	187–215	222–273	74–141	125–183	3–253
	2–315	84–187	252–253	74–222	43–183	69–175	153–209	72–315	163–187	208–253
	89–153	273–324	2–163	2–72	2–84	84–253	166–253	153–163	175–253	66–215
	125–253	3–82	43–187	43–73	69–190	2–43	43–253			
Task 3 (38)	187–189	183–253	69–269	186–189	73–128	189–271	267–290	132–141	74–183	74–189
	186–187	82–187	267–273	194–209	141–194	183–186	82–190	187–190	194–208	84–141
	170–194	141–193	160–193	120–141	141	132–153	68–141	73–189	112–209	73–82
	35–194	35–73	146–187	267–315	187–252	166–209	187–215	187–315		
Task 4 (32)	71–162	45–211	120–272	56–112	38–47	47–71	38–211	47–250	211–298	32–43
	17–260	162–260	84–228	155–228	271–283	168–170	211–250	17–47	94–129	38–250
	72–134	84–215	3–228	32–47	43–72	211–260	72–250	32–276	161–271	61–168
	129–222	94–1								
Task 5 (43)	43–130	35–186	36–130	89–129	207–260	109–209	129–166	36–129	35–178	38–45
	74–156	138–183	120–128	83–109	43–129	71–129	179–239	71–179	183–187	84–262
	127–239	19–187	61–178	85–161	19–69	35–205	179–209	51–179	128–197	191–274
	83–262	197–227	3–197	36–209	161–19	89–239	73–178	166–179	128–186	35–170
	96–127	209–298	183–190							

Note: The number after Task No. is the important feature number.

Abbreviation: MP=matching pursuit method.

TABLE 7. Antigenic sites and corresponding amino acid positions within the HA1 epitope identified as critical for antigenic changes across tasks based on the MP model.

Antigenic sites	Task 1-aa	Task 2-aa	Task 3-aa	Task 4-aa	Task 5-aa
Sa	121, 153, 157, 160	125, 153, 163	120, 153, 160	120, 155, 161, 162	120, 156, 161
Sb	186, 187, 193	187, 190, 208, 209	186, 187, 189, 190, 193, 194, 208, 209	186, 211	186, 187, 190, 191, 197, 207, 209
Ca	141, 216, 222	141, 166, 215, 222	141, 146, 166, 170, 215, 222	142, 168, 170, 215, 216, 222	138, 166, 170, 205, 239
Cb	54, 71, 74, 253	72, 73, 74, 82, 84, 89, 253	68, 73, 74, 82, 84, 253	71, 72, 84, 260	71, 73, 74, 84, 85, 89, 260, 262
Pa	272	43, 273	43, 269, 271, 273	43, 271, 276, 283	43, 274
Pb	36		35, 290	38	35, 36, 38

Abbreviation: MP=matching pursuit method; HA=hemagglutinin.

DISCUSSION

This article introduces a novel approach for predicting antigenic variations of H1N1 influenza A — the MP model. Traditionally, antigenic variation prediction relies on extracting protein sequences and serological data, followed by applying regression-based models to infer the antigenic characteristics of novel viral protein sequences. In contrast, this study incorporates AFD theory as a key component, offering an alternative analytical perspective that aims to enhance predictive performance and interpretability.

The proposed method demonstrates several significant advantages. First, the algorithm leverages AFD to dynamically select optimal basis functions, which enhances its capacity to capture nonlinear relationships in antigenic data. This flexibility

effectively mitigates issues such as overfitting, a common challenge in high-dimensional datasets with sparse labels. Second, compared with traditional regression techniques, the model offers improved interpretability, superior computational efficiency, and reduced complexity, making it particularly suitable for large datasets and real-time applications. Furthermore, the model's applicability extends beyond H1N1 influenza A, with preliminary results suggesting its utility for other influenza subtypes such as H3N2 and Influenza B, and its potential adaptability to other viral families. Notably, this study also incorporates dual-site synergy considerations, identifying key site interactions from five publicly available datasets.

Empirical evaluations on these datasets indicate that the model performs well across various metrics, often outperforming baseline methods. However, deeper

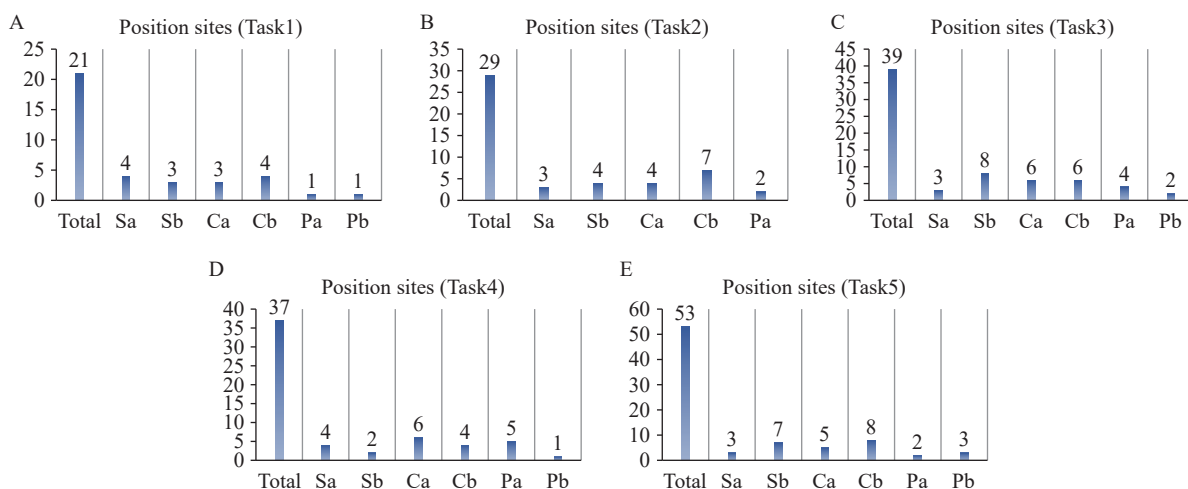


FIGURE 5. Bar charts illustrating the distribution of identified amino acid mutations across antigenic sites (Sa, Sb, Ca, Cb, Pa, and Pb) for (A–E) Tasks 1–5.

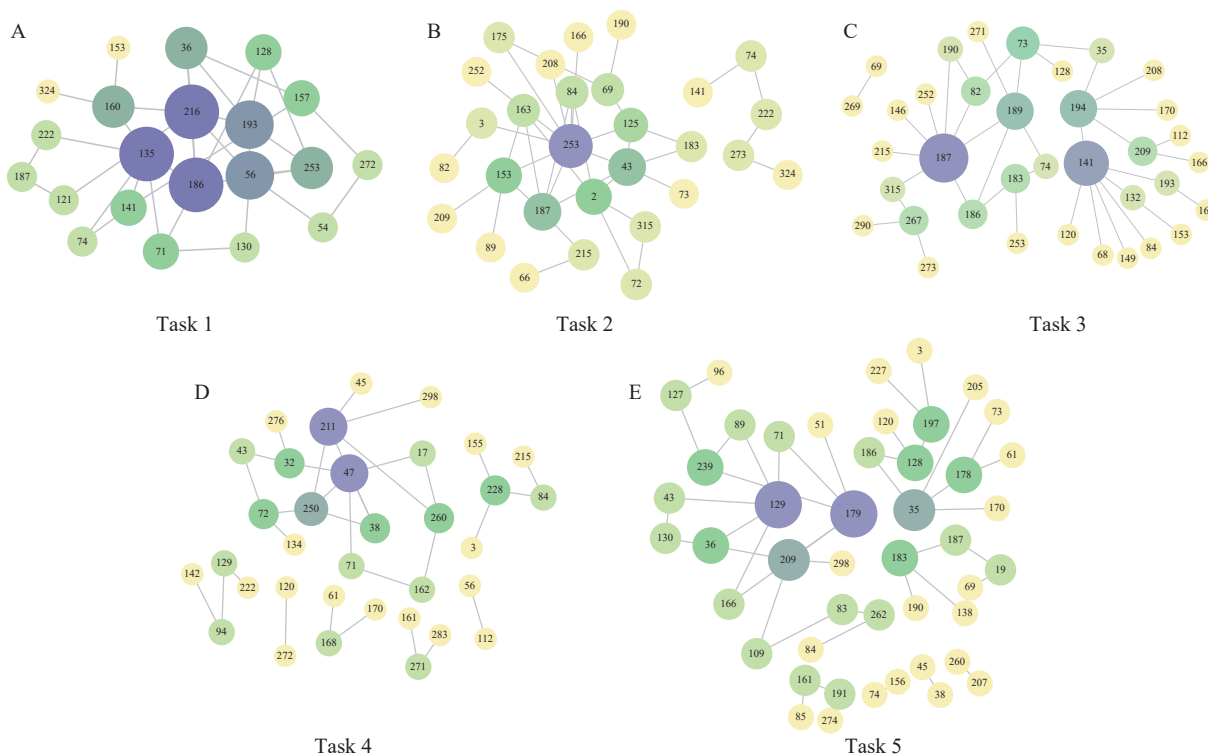


FIGURE 6. Network diagram of two-site interactions for (A–E) Task 1–5.

analysis has revealed certain areas requiring improvement. For example, while the algorithm exhibits strengths in computational efficiency and generalization, its sensitivity to capturing subtle antigenic shifts could be further refined.

Future efforts will focus on integrating advanced feature engineering to capture domain-specific viral protein properties and exploring ensemble learning to enhance predictive robustness. We also plan to collaborate with virology experts on cell-based

experiments to validate our predictions and support applications in vaccine design and epidemiological forecasting. This comprehensive approach aims to refine our methodology and contribute to addressing complex challenges in influenza and broader virology research.

Conflicts of interest: No conflicts of interest.

Funding: Supported by Major Project of Guangzhou National Laboratory, (Grant No. GZNL2024A01004), the National Natural Science

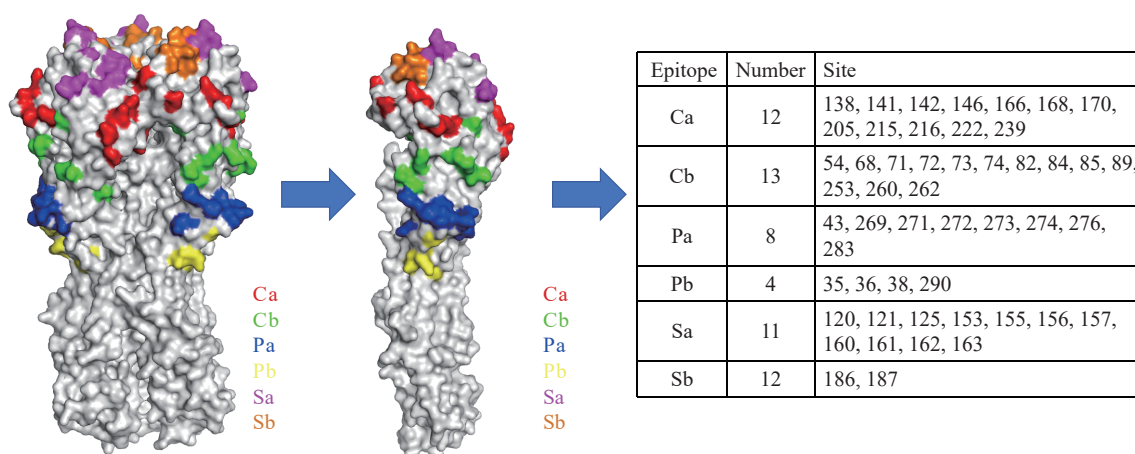


FIGURE 7. The selected amino acids of six antigenic sites (i.e., Ca, Cb, Pa, Pb, Sa, and Sb) of H1 (A/California/04/2009; PDB 3UBE).

Foundation of China (Grant No. 82361168672), the Science and Technology Development Fund of Macau SAR (Grant No. FDCT 0111/2023/AFJ, 0155/2024/RIA2, 005/2022/ALC, 0128/2022/A, 0020/2023/RIB1), National Key Research and Development Program of China (Grant No. 2024YFE0214800), Self-supporting Program of Guangzhou Laboratory (Grant No. SRPG22-007), National Key Research and Development Program of China (Grant No. SQ2024YFE0202244), Engineering Technology Research (Development) Center of Ordinary Colleges and Universities in Guangdong Province (Grant No. 2024GCZX010).

doi: 10.46234/ccdcw2025.078

* Corresponding authors: Tao Qian, tqian@must.edu.mo; Chitin Hon, chthon@must.edu.mo; Zifeng Yang, yang_zifeng@gzlab.ac.cn.

¹ State Key Laboratory of Respiratory Disease, National Clinical Research Center for Respiratory Disease, Guangzhou Institute of Respiratory Health, The First Affiliated Hospital of Guangzhou Medical University, Guangzhou City, Guangdong Province, China; ² College of Sciences, China Jiliang University, Hangzhou City, Zhejiang Province, China; ³ Department of Engineering Science, Faculty of Innovation Engineering, Macau University of Science and Technology, Macao Special Administrative Region, China; ⁴ Guangzhou National Laboratory, Guangzhou City, Guangdong Province, China; ⁵ Guangzhou key laboratory for clinical rapid diagnosis and early warning of infectious diseases, KingMed School of Laboratory Medicine, Guangzhou Medical University, Guangzhou City, Guangdong Province, China; ⁶ Engineering Technology Research Center of Intelligent Diagnosis for Infectious Diseases in Guangdong Province, Guangzhou City, Guangdong Province, China; ⁷ Guangdong Provincial Engineering Research Center for Early Warning and Diagnosis of Respiratory Infectious Diseases, Guangzhou City, Guangdong Province, China; ⁸ Department of Electrical Engineering & Computer Science, College of Engineering, University of Missouri, Columbia, MO, USA; ⁹ Respiratory Disease AI Laboratory on Epidemic and Medical Big Data Instrument Applications, Faculty of Innovation Engineering, Macau University of Science and Technology, Macao Special Administrative Region, China; ¹⁰ Macau Center for Mathematical Sciences, Macau University of Science and Technology,

Macao Special Administrative Region, China.

* Joint first authors.

Copyright © 2025 by Chinese Center for Disease Control and Prevention. All content is distributed under a Creative Commons Attribution Non Commercial License 4.0 (CC BY-NC).

Submitted: December 12, 2024

Accepted: March 28, 2025

Issued: April 04, 2025

REFERENCES

- World Health Organization. Influenza (seasonal). 2024. [https://www.who.int/news-room/fact-sheets/detail/influenza-\(seasonal\)](https://www.who.int/news-room/fact-sheets/detail/influenza-(seasonal)). [2024-8-30].
- Krammer F, Smith GJD, Fouchier RAM, Peiris M, Kedzierska K, Doherty PC, et al. Influenza. *Nat Rev Dis Primers* 2018;4(1):3. <https://doi.org/10.1038/s41572-018-0002-y>.
- Carrat F, Flahault A. Influenza vaccine: the challenge of antigenic drift. *Vaccine* 2007;25(39-40):6852 - 62. <https://doi.org/10.1016/j.vaccine.2007.07.027>.
- CDC. CDC's World Health Organization (WHO) collaborating center for surveillance, epidemiology and control of influenza. 2024. <https://www.cdc.gov/flu/php/who-collaboration/index.html>. [2024-8-6].
- Houser K, Subbarao K. Influenza vaccines: challenges and solutions. *Cell Host Microbe* 2015;17(3):295 - 300. <https://doi.org/10.1016/j.chom.2015.02.012>.
- Liao YC, Lee MS, Ko CY, Hsiung CA. Bioinformatics models for predicting antigenic variants of influenza A/H3N2 virus. *Bioinformatics* 2008;24(4):505 - 12. <https://doi.org/10.1093/bioinformatics/btm638>.
- Li L, Chang D, Han L, Zhang XJ, Zaia J, Wan XF. Multi-task learning sparse group lasso: a method for quantifying antigenicity of influenza A (H1N1) virus using mutations and variations in glycosylation of Hemagglutinin. *BMC Bioinformatics* 2020;21(1):182. <https://doi.org/10.1186/s12859-020-3527-5>.
- Sun HL, Yang JL, Zhang T, Long LP, Jia K, Yang GH, et al. Using sequence data to infer the antigenicity of influenza virus. *mBio* 2013;4(4):e00230 - 13. <https://doi.org/10.1128/mBio.00230-13>.
- Qu W, Hon CT, Zhang YQ, Qian T. Matrix pre-orthogonal matching pursuit and pseudo-inverse. *arXiv preprint arXiv:2412.05878*, 2025.
- Hon C, Liu ZG, Qian T, Qu W, Zhao JM. Trends by adaptive Fourier decomposition and application in prediction. *Int J Wavelets, Multiresolut Inf Process* 2024;22(5):2450014. <https://doi.org/10.1142/S0219691324500140>.

SUPPLEMENTARY MATERIAL

Data Description

This study utilized serologic data for H1N1 viruses, comprising 2,030 HI titers generated from 153 viruses and 97 serum samples, along with 13,591 non-identical amino acid sequences of HA proteins, accessible at <https://github.com/InfluenzaSystemsBiology/MTL-SGL>. Analysis of swine-origin influenza viruses (SOIVs) collected from humans between 1990 and 2010 revealed that their HA and neuraminidase (NA) genes belong to the triple-reassortant swine-origin influenza virus (tr-SOIV) lineage, which evolved from classical swine-origin influenza virus (cSOIV) A(H1N1). The tr-SOIV HA genes form two distinct clusters: H1gamma (predominantly east of the Mississippi River) and H1beta (west of the Mississippi River). Seasonal human H1N1 viruses (1977–2009) were characterized using HI assays, involving 115 virus isolates, 77 serum isolates, and 1,882 measurements to correlate antigenic dynamics with molecular evolution. Additionally, swine H1N1 viruses from 2008 were characterized through genome sequencing and serological cross-reactivity analysis to elucidate genetic diversity and antigenic properties.

Our analysis incorporated five datasets, denoted as (A_1, Y_1) , (A_2, Y_2) , (A_3, Y_3) , (A_4, Y_4) , (A_5, Y_5) . Matrices A_m represent HA protein sequences, while vectors Y_m represent antigenic distances, where $m = 1, \dots, 5$. The dimensions of A_m are 78×167 , 861×167 , $4,950 \times 167$, 91×167 , and 276×167 , respectively. The dimensions of vectors Y_m correspond to the number of rows in matrix A_m . For each dataset, amino acid substitutions and antigenic distances for virus pairs were determined using established protocols. Specifically, amino acid substitutions were quantified using a binary coding schema for all HA sequence pairs. Antigenic distances for corresponding virus pairs were calculated based on their HI titers against different antisera using a low-rank matrix completion method. Each dataset was randomly partitioned into two segments: 70 percent allocated for model training to establish underlying patterns and relationships, and the remaining 30 percent reserved as a testing set to evaluate model performance on unseen data.

Formulation of Matching Pursuit Model

Suppose $A = (a_1, a_2, \dots, a_p)$, where $a_l \in \mathbb{R}^q$, $l = 1, 2, \dots, p$, are the non-zero column vectors of A and \mathbb{R}^q is the Euclidean space with dimension q . Let $Y \in \mathbb{R}^q$. Leveraging the idea of polynomial regression, we perform feature expansion on A . Through feature expansion, the elements of A can be transformed into higher-order features such as squared terms, cubic terms, or even higher-order terms. Additionally, this process includes interaction terms between the elements of A , known as feature interactions. This enhancement significantly boosts the model's expressive power, enabling us to effectively capture complex nonlinear relationships when addressing real-world problems. Without loss of generality, we still use the notation $A = (a_1, a_2, \dots, a_p)$ to represent the result after completing the feature extension.

The objective is to identify a re-ordered subset of A , denoted as $A = (a_{l_1}, \dots, a_{l_p})$, $p' \leq p$, and a row vector $X = (x_1, \dots, x_{p'})$ such that

$$\|Y - AX^t\|$$

is minimized, where $\|\cdot\|$ is the Euclidean norm and X^t is the transpose of X .

Let $B = (b_1, b_2, \dots, b_p)$ be the normalization of vectors A , i.e., $b_l = a_l / \|a_l\|_2$, $l = 1, 2, \dots, p$. Denote by Q_{bl} the Gram-Schmidt orthogonalization with respect to any vector bl . That is

$$Q_{bl}(a_l) = a_l - \langle a_l, b_l \rangle b_l.$$

For a set of p orthogonal vectors $B = b_1, \dots, b_p$, the following relationship holds:

$$Q_{b_p}(Q_{b_{p-1}}(\dots(Q_{b_1}(a_l))\dots)) \triangleq Q_{b_p} \circ Q_{b_{p-1}} \circ \dots \circ Q_{b_1}(a_l)$$

Corresponding to the description in Section 2, we consider A as the kernel functions, B as the normalized kernel functions, and B as the Takenaka-Malmquist system. Through this framework, we can apply the discrete form of the maximal selection principle (MSP).

For the initial case where $l = 1$, we select I_1 and a_{1I_1} according to:

$$\operatorname{argmax}\left\{\left\langle Y, \frac{a_k}{\|a_k\|} \right\rangle^2 : k = 1, \dots, p\right\}$$

We then set $b_1 = \frac{a_1}{\|a_1\|}$ and $b_k^l = b_k^1 = Q_{b_1}(a_k^{l-1}) = Q_{b_1}(a_k^0), k = 1, \dots, p,$ where we adopt the notation $a_k^0 = a_k$. This yields the first parameter $x_1 = \langle Y, b_1 \rangle$ for our model, where $\langle \cdot, \cdot \rangle$ represents the Euclidean inner product.

Next, we discuss $l = 2$. Select I_2 and a_{I_2} according to

$$\operatorname{argmax}\left\{\left\langle Y, \frac{b_k^1}{\|b_k^1\|} \right\rangle^2 : k = 1, \dots, p\right\}$$

Naturally, $I_2 \neq I_1$. If the maximum value is zero, the selection process terminates at this step. Otherwise, set $b_1 = \frac{b_{I_2}^1}{\|b_{I_2}^1\|}$ and $b_k^l = b_k^2 = Q_{b_2}(b_k^1), k = 1, \dots, p$. Furthermore, we derive the second parameter $x_2 = \langle Y, b_2 \rangle$ for our model.

Inductively, for any integer $l > 2$, we ultimately obtain an orthonormal system $b_1, \dots, b_{p'}$ and an integer $p' \leq p$, where p' can be computed by

$$\operatorname{argmax}\left\{\left\langle Y, \frac{b_k^p}{\|b_k^p\|} \right\rangle^2 < \epsilon : k = 1, \dots, p\right\}$$

for a predetermined ϵ . Controlling the sample size (i.e., the size of q), along with feature expansion, ensures that the integer $p' (\leq p)$ is attained. Denote by $X = (x_1, \dots, x_{p'})$, where $x_l = \langle Y, b_l \rangle, l = 1, \dots, p'$. Additionally, we have

$$b_l = \frac{Q_{b_{l-1}} \circ \dots \circ Q_{b_1}(a_{I_l}^0)}{\|Q_{b_{l-1}} \circ \dots \circ Q_{b_1}(a_{I_l}^0)\|} = \frac{Q_{b_{I_l}}(b_{I_l}^{l-2})}{\|Q_{b_{l-1}}(b_{I_l}^{l-2})\|}, l = 3, \dots, p'.$$

Denote by A the $q \times p'$ matrix formed by the column vectors $(a_{I_1}, \dots, a_{I_{p'}})$ in the ordered sequence $I = (I_1, \dots, I_{p'})$, and $B = (b_1, \dots, b_{p'})$. Let $W_{p' \times p'}$ represent the transformation matrix between A and B , where B is orthonormal. Therefore, the matching pursuit model is formulated as

$$Y = B X^* = (A W) X^* = A W$$

which provides a solution to $\|Y - AX^*\|$, where $W = W X^*$ represents the coefficient vector expressed in terms of the basis A .

The formulation of this model is grounded in AFD theory and derives its strength from effectively modeling nonlinear systems. Unlike conventional methods constrained by predetermined basis functions, our matching pursuit model dynamically selects the most appropriate functions from a dictionary to efficiently capture the complexities of nonlinear signals. Furthermore, as nonlinear systems typically contain substantial redundant information, our approach employs the Matching Pursuit algorithm to iteratively approximate the signal. By selectively incorporating only dictionary elements that significantly contribute to the signal's energy, we achieve a sparse approximation. Additionally, by leveraging high-order polynomials, we incorporate synergistic interactions between features through the inclusion of feature products (higher-order features). With this extended dictionary comprising higher-order features, the antigenic distance can be precisely determined and subsequently used for prediction through the sequential maximal selection of columns in the consecutively obtained orthogonal complements.

Prediction Procedure

Suppose we have two pairs of data, consisting of sequence data and antigenic data, denoted as (A, Y) and (A_1, Y_1) , respectively. We use (A, Y) as the training set and (A_1, Y_1) as the testing set. Based on the matching pursuit model [3] established in the previous section, once the training set has been processed, we can derive two key outputs: the parameter set $W = W X^*$ and the index set $I = (I_1, \dots, I_{p'})$.

Methods and Applications

Development of A Novel EvaGreen-Dye Based Recombinase Aided Amplification Assay Using Self-Avoiding Molecular Recognition System Primers

Xinxin Shen¹; Shaowei Hua¹; Zijin Zhao¹; Fengyu Tian¹; Lingjun Li^{2*}; Xuejun Ma^{1,#}

ABSTRACT

Introduction: Fluorescent probe-based recombinase aided amplification (RAA) offers the advantages of rapidity and simplicity but is limited by the requirement for complex and lengthy probe design, restricting its widespread application.

Methods: A novel EvaGreen dye-based RAA (EvaGreen-RAA) assay utilizing self-avoiding molecular recognition system (SAMRS) primers was developed for the detection of *Pseudomonas fluorescens* (PF) and *Bacillus cereus* (BC) in milk. Conventional RAA was used as a reference method. Sensitivity was evaluated using nucleic acids from recombinant plasmids and simulated milk specimens. Additionally, a dual EvaGreen-RAA assay was investigated for simultaneous detection of mixed BC and PF in simulated milk specimens.

Results: The EvaGreen-RAA demonstrated superior sensitivity compared to conventional RAA, with detection limits of 1 copy/ μ L versus 10 copies/ μ L for both BC and PF plasmids, respectively. In simulated milk specimens, EvaGreen-RAA detected BC and PF at concentrations of 100 CFU/mL and 200 CFU/mL, respectively, compared to 400 CFU/mL and 600 CFU/mL for conventional RAA. The dual EvaGreen-RAA assay successfully detected mixed BC and PF in simulated milk specimens at concentrations of 200 CFU/mL for each pathogen.

Conclusion: The EvaGreen-RAA assay demonstrated significant advantages in terms of simplicity and enhanced sensitivity compared to fluorescent probe-based RAA, offering a novel approach for developing multiplex pathogen detection systems using melting curve analysis.

Pseudomonas fluorescens (PF) is one of the primary bacterial agents responsible for spoilage and

deterioration of milk and eggs during low-temperature storage, and can lead to shock following human infection in severe cases (1). *Bacillus cereus* (BC) represents the most prevalent foodborne pathogen in raw milk and dairy farm environments (2). Both bacteria commonly contaminate dairy products as psychrophiles; when humans consume dairy products contaminated with these psychrophiles, they can experience vomiting, diarrhea, and various other illnesses (3). With the increasing recognition of protein's nutritional importance, milk has become an indispensable food source for organisms that require external protein intake (4).

Currently, most quality inspection departments in dairy enterprises employ traditional culture methods for pathogen detection, a process requiring culture, isolation, purification, and biochemical and serological identification. This approach typically requires 5–7 days before results are available, with exceedingly complex and time-consuming detection steps. PCR-based molecular methods have also been implemented for pathogen diagnosis in dairy products, reducing detection time to 1–2 hours, but these methods require relatively complex thermal cycling instruments and operational procedures. In recent years, isothermal amplification technologies have gained widespread acceptance due to their time efficiency, eliminating the need for complex temperature cycling processes (5). Recombinase aided amplification (RAA) offers high sensitivity and specificity, completing nucleic acid amplification at 37–42 °C within 20–30 min; however, a significant limitation of RAA is the requirement for designing complex and lengthy probes (45 nucleotides in length) (6–7). Although dye-based isothermal amplification methods without fluorescent probes allow result visualization, these approaches exhibit reduced specificity due to non-specific binding of dyes to double-stranded DNA.

The self-avoiding molecular recognition system (SAMRS) employs nucleotide analogs A*, G*, C*, and

T* to substitute for A, G, C, and T at specific positions within primers, where A* pairs with T, T* pairs with A, G* pairs with C, and C* pairs with G. Additionally, SAMRS primers can bind to normal single-stranded DNA. Since SAMRS primers do not bind to each other, the formation of primer dimers can be minimized or even eliminated (8).

In this study, we replaced several bases at the 3' terminus of standard RAA primers with unnatural bases to create SAMRS primers and developed an EvaGreen-RAA assay for BC and PF detection using these SAMRS primers. This approach enables real-time observation of reaction results within 30 minutes while eliminating the need to design complex RAA probes, thereby maintaining the sensitivity and specificity of the RAA assay.

METHODS

Strain Collection and Nucleic Acid Extraction

Standard strains of *Bacillus cereus* (ATCC13525) and *Listeria monocytogenes* (ATCC11778) were purchased from the BeNa Culture Collection. Nucleic acid was extracted using the FastPure[®] Microbiome DNA Isolation Kit (Vazyme Biotech, Nanjing, China).

The Preparation Process of SAMRS Nucleotides

All intermediates and final products were characterized by ¹H NMR (Nuclear Magnetic Resonance) or ³¹P NMR, with spectral data consistent with previously reported findings (9). All

oligonucleotides containing modified nucleobases were synthesized by Sangon Biotech.

Primer and Probe Design

The B subunit of the DNA gyrase gene (*gyrB*) and alkaline metalloprotease gene (*aprX*) were selected as specific targets for the identification of BC and PF, respectively. Highly conserved regions of *gyrB* and *aprX* genes were downloaded from NCBI GenBank and subjected to sequence alignment using BioEdit software. The designed primers and probes were evaluated using Oligo7 and Amplifx software. The specific sequences of primers and probes are presented in Table 1.

Construction of Recombinant Plasmids

The target fragments of *gyrB* and *aprX* genes were cloned into pUC57 vector for the construction of recombinant plasmids, respectively, which were synthesized by TsingKe Biotech Crop (Beijing, China). Plasmids were quantified using the Qubit[®] dsDNA HS Assay Kit (Thermo Fisher Scientific, Waltham, MA, United States), and the copy number per microliter was calculated according to the equation: copies/reaction = $[(6.02 \times 10^{23}) \times \text{concentration (ng/}\mu\text{L)} \times 10^{-9}] / [\text{number of bases (bp)} \times 660]$. The lyophilized plasmids were reconstituted by adding 40 μL of TE buffer, quantified, and stored at $-80\text{ }^{\circ}\text{C}$ until use.

Establishment of RAA and EvaGreen-RAA

The RAA reaction was performed in a total volume of 50 μL , containing a dry powder pellet, 2 μL of RAA standard nucleotide (STD) primer, 4 μL of betaine, 0.6

TABLE 1. Primer and probe sequences used in this study.

Primer/probe	Sequence (5'–3')	Length	Amplicon size (bp)
BC-RAA-F	GTA A A T C C A T T A C C A A A A A T A C G A A A G A G G	31	167
BC-SAMRS-F	G T A A A A T C C A T T A C C A A A A A T A C G A A A * G * A * G * G	31	
BC-RAA-R	T T C A C G C A T A C G A G T T G C T A G C G T A T C A A A	30	
BC-SAMRS-R	T T C A C G C A T A C G A G T T G C T A G C G T A * T C * A * A * A	30	
BC-RAA-P	T C A T T G G T G A C A C C G A T C A A A C A G G A A C R A / i 6 F A M d T / A / i d S p / C / i B H Q 1 d T / C G A T T T A A C C A G A T - C 3	49	
PF-RAA-F	C G G C A A C C C G A C C T A T A A C G A C G C A A C C T A	30	177
PF-SAMRS-F	C G G C A A C C C G A C C T A T A A C G A C G C A * A * C * C * T A	30	
PF-RAA-R	T T G G C A C C G T A G A G C T T C T G G A T C G C C G C A A T	32	
PF-SAMRS-R	T T G G C A C C G T A G A G C T T C T G G A T C G C C G * C * A * A * T	32	
PF-P	C A G G A C A C G C G T G G C T A T A G C C T C A T G A G T / i 6 F A M d T // i d S p / C / i B H Q 1 d T / G G A G C G A G A G C A A C A C - C 3	49	

Abbreviation: SAMRS=self-avoiding molecular recognition system; RAA=recombinase aided amplification; FAM=6-carboxyfluorescein; THF=tetrahydrofuran; BHQ=black hole quencher; C3-spacer=3'phosphate blocker; A*, G*, and C* =SAMRS nucleotides.

μL of probe, 5 μL of template, and 29.4 μL of reaction buffer (Amp-Future, Changzhou, China). Additionally, 2.5 μL of magnesium acetate (280 mmol/L) was added to the reaction lid as an initiator for the RAA reaction, followed by brief centrifugation to ensure rapid reaction initiation at 39 °C for 30 min.

The EvaGreen RAA reaction differed from the standard protocol by the addition of 2.5 μL of EvaGreen dye, 2 μL of betaine, and 1.2 μL each of SAMRS forward and reverse primers (10 μmol/L). All other reagents remained identical to those described above.

Assessing the Ability of SAMRS Primers to Reduce Primer Dimerization

Serial dilutions of recombinant plasmids (10^1 – 10^6 copies/μL) were used as templates for probe-free RAA reactions with both STD and SAMRS primers for BC and PF at 39 °C for 30 min. Following amplification, products underwent a melting curve analysis from 60 to 95 °C with a temperature gradient of 0.2 °C/s. Fluorescence signals were detected in the SYBR green channel, and high-resolution melting curves (HRM) were generated by plotting the negative inverse of fluorescence values against temperature. In addition to HRM analysis, primer dimer formation was evaluated using agarose gel electrophoresis (AGE).

Sensitivity and Specificity of RAA and EvaGreen-RAA assays

To validate the sensitivity of both RAA and EvaGreen RAA assays, serial dilutions of BC or PF recombinant plasmids (10^0 – 10^5 copies/reaction) were used as templates, with DEPC water serving as a negative control. Each reaction was performed in eight replicates.

The specificity of both assays was evaluated using 18 common foodborne pathogens, including BC (ATCC11778), PF (ATCC13525), *Staphylococcus aureus* (ATCC29213), *Listeria monocytogenes* (ATCC19115), *Pseudomonas aeruginosa* (ATCC27853), *Klebsiella pneumoniae* (ATCC11296), *Escherichia coli* (isolated strains), *Staphylococcus epidermidis* (isolated strains), *Enterococcus faecium* (isolated strains), *Enterococcus faecalis* (isolated strains), *Enterobacter cloacae* (isolated strains), *Pseudomonas maltophilia* (isolated strains), *Proteus mirabilis* (isolated strains), *Candida albicans* (ATCC753), *Candida tropicalis* (ATCC750), *Candida parapsilosis* (ATCC22019), *Candida glabrata* (ATCC2001), and

Candida krusei (ATCC6258). DEPC water was used as a negative control, with each reaction performed in eight replicates.

Preparation of Simulated Milk Specimens and Detection

Standard BC and PF strains were inoculated into Nutrient Broth (NB) and Luria-Bertani (LB) liquid media, respectively, and cultured overnight on a shaker. Bacterial suspensions were quantified spectrophotometrically, with OD values between 0.45–0.5 corresponding to approximately 10^8 CFU/mL. The accuracy of spectrophotometric quantification was verified by direct microscopic enumeration using a bovine abalone blood counting chamber. Following sequential ten-fold dilutions, appropriate bacterial concentrations were added to sterilized milk to prepare simulated specimens. Nucleic acids were extracted from these specimens, and both fluorescent RAA and EvaGreen RAA assays were performed in parallel to determine their respective detection sensitivities.

Dual EvaGreen-RAA Assay for Mixed BC and PF in Simulated Milk Specimens Using Melting Curves

The dual EvaGreen-RAA reaction system comprised 29.4 μL of buffer, 1 μL each of SAMRS forward and reverse primers for PF and BC, 2.5 μL of EvaGreen dye, 2 μL of betaine (5 mol/L), 2.5 μL of magnesium acetate (280 μmol/L), and 2.5 μL of templates (corresponding to 200 CFU/mL) for each BC and PF. The RAA reaction was initially performed at 39 °C for 30 min, followed by high-resolution melting curve analysis on a PCR instrument.

RESULTS

SAMRS Primers Reduced or Eliminated Primer Dimerization

When STD primers were used in the RAA system, both high product peaks and non-specific primer dimer peaks at approximately 30–35 °C were observed (Figure 1A and 1E). In contrast, SAMRS primers produced only distinct high product peaks at 84 °C and 91 °C, with complete elimination of non-specific product peaks (Figure 1B and 1F). To validate these findings, amplification products from both methods

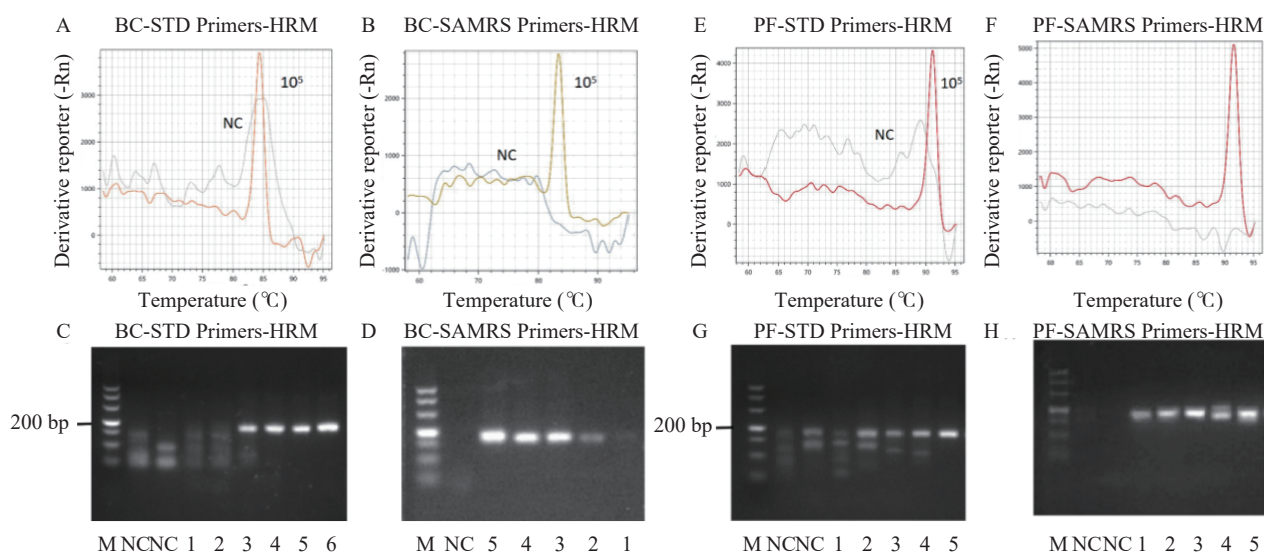


FIGURE 1. Effect of SAMRS primers on primer dimerization. (A) Merged HRM results of the STD primer for BC; (B) Merged HRM results of SAMRS primers for BC; (C) Merged HRM results of the STD primer for PF; (D) Merged HRM results of SAMRS primers for PF; (E) AGE results of STD primers for BC; (F) AGE results of SAMRS primers for BC; (G) AGE results of STD primers for PF; (H) AGE results of SAMRS primers for PF.

Note: Lane M: Marker; Lanes 1–6: 10^1 , 10^2 , 10^3 , 10^4 , 10^5 and 10^6 copies/ μ L BC or PF recombinant plasmids.

Abbreviation: SAMRS=self-avoiding molecular recognition system; AGE=agarose gel electrophoresis; STD=standard nucleotide; HRM=high-resolution melting curves; NC=negative control; BC=*Bacillus cereus*; PF=*Pseudomonas fluorescens*.

were analyzed by agarose gel electrophoresis (3%). STD primers generated prominent dimer bands (Figure 1C and 1G), whereas SAMRS primers yielded no detectable dimer formation (Figure 1D and 1H). These results conclusively demonstrate that incorporating SAMRS primers into the RAA reaction system effectively inhibited or completely eliminated primer dimer formation.

Sensitivity of RAA and EvaGreen-RAA Assays Using Recombinant Plasmids and Simulated Milk Specimens

The sensitivity of the RAA reaction was 10 copies/ μ L for both BC and PF (Figure 2A and 2B), while the EvaGreen-RAA reaction demonstrated enhanced sensitivity at 1 copy/ μ L for both pathogens using recombinant plasmids (Figure 2C and 2D). In simulated milk specimens, the detection sensitivity of the RAA assay for BC and PF was 400 CFU/mL and 600 CFU/mL (Figure 2E and 2F), respectively, whereas the EvaGreen-RAA assay exhibited superior sensitivity at 100 CFU/mL and 200 CFU/mL (Figure 2G and 2H), respectively. These results demonstrate that the utilization of SAMRS primers consistently achieves enhanced detection sensitivity compared to STD primers in equivalent assay conditions.

Specificity of RAA and EvaGreen-RAA Assays Using Common Foodborne Pathogens

Both the RAA and EvaGreen-RAA assays demonstrated high specificity for BC and PF detection, with no cross-reactivity observed against 16 other common foodborne pathogens (Table 2).

Dual EvaGreen-RAA Assay for Mixed BC and PF in Simulated Milk Specimens Using Melting Curves

Amplification products with distinct nucleotide compositions exhibit characteristic melting temperature (T_m) values. High-resolution melting curve analysis of the dual EvaGreen-RAA amplification products revealed two clearly distinguishable product peaks at 84 °C and 91 °C (Figure 3). These distinct peaks corresponded precisely to the individual melting curves of BC and PF, demonstrating that the EvaGreen-RAA assay with HRM analysis can effectively identify and differentiate mixed BC and PF contamination in simulated milk specimens at concentrations as low as 200 CFU/mL for each pathogen.

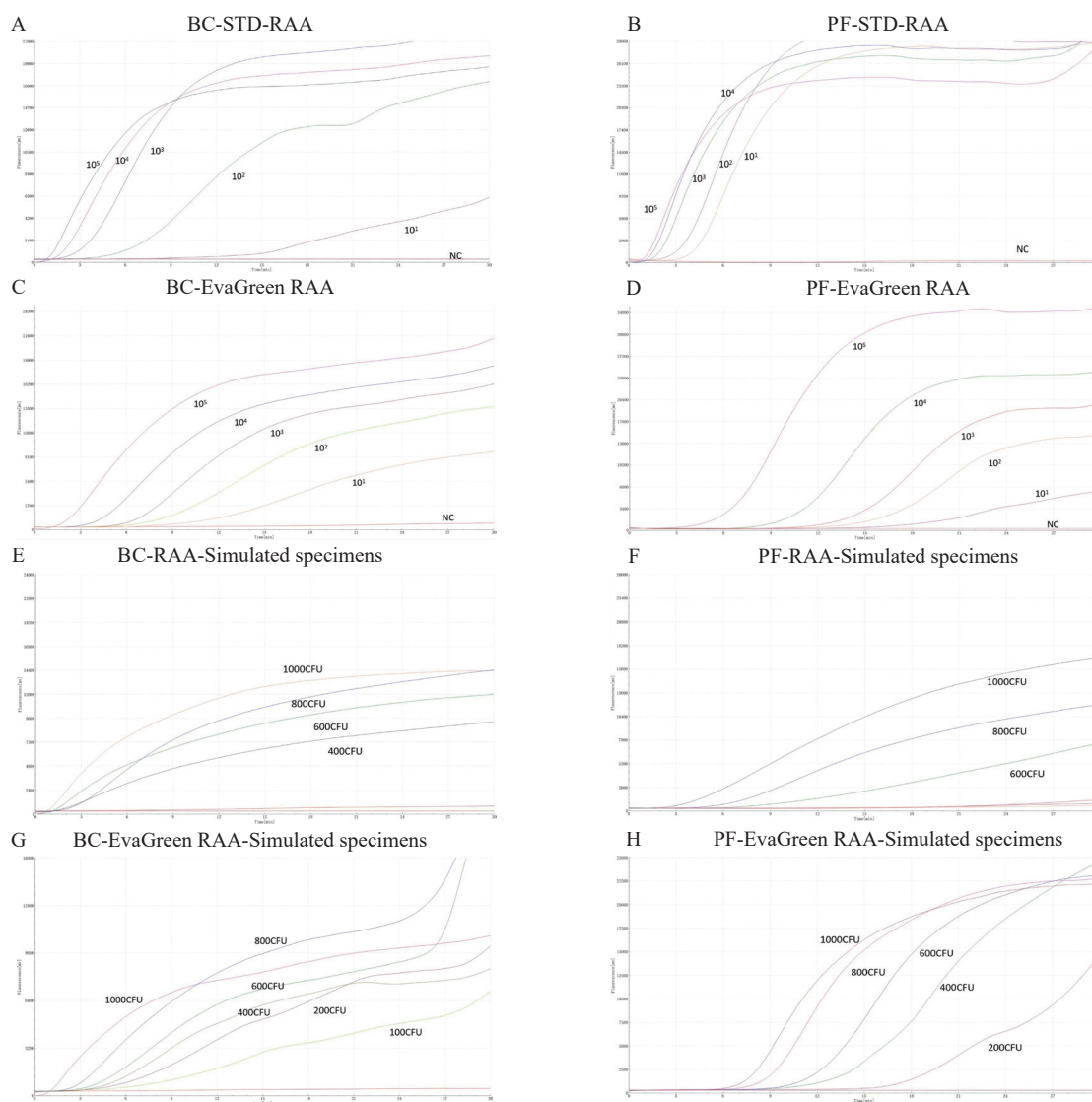


FIGURE 2. Sensitivity assessment of RAA and EvaGreen-RAA on recombinant plasmids. (A) The sensitivity of RAA for BC was 10 copies/ μL ; (B) The detection sensitivities of RAA for PF was 10 copies/ μL ; (C) The sensitivity of EvaGreen-RAA for BC was 1 copy/ μL ; (D) The detection sensitivities of EvaGreen-RAA for PF was 1 copy/ μL . Detection of RAA and EvaGreen-RAA on simulated milk specimens; (E) The detection sensitivity of RAA for BC in simulated specimens was 400 CFU/mL; (F) The detection sensitivity of RAA for PF in simulated specimens was 600 CFU/mL; (G) The detection sensitivity of EvaGreen-RAA for BC in simulated specimens was 100 CFU/mL; (H) The detection sensitivity of EvaGreen-RAA for PF in simulated specimens was 200 CFU/mL.

Abbreviation: RAA=recombinase aided amplification; BC=*Bacillus cereus*; PF=*Pseudomonas fluorescens*.

DISCUSSION

While probe-based RAA fluorescence assays demonstrate sensitivity and specificity comparable to real-time PCR, they require probes of considerable length (45–52 bp) with a tetrahydrofuran site positioned centrally within the sequence. These requirements substantially increase both the complexity of probe design and associated costs, particularly when targeting highly variable pathogens.

Furthermore, multiplexed RAA reactions present significant challenges due to interference between different probe and primer sets within a single reaction vessel.

Previous investigations have demonstrated the utility of SAMRS in various isothermal amplification techniques, including recombinant polymerase amplification (RPA) and deconjugate-dependent amplification (HDA), where strategic placement of SAMRS nucleotides at the 3' end of primer-binding sites effectively prevents the formation of most primer

TABLE 2. Bacterial strains used in the specificity test.

Strains and origins	RAA (BC)	EvaGreen-RAA (BC)	RAA (PF)	EvaGreen-RAA (PF)
<i>Bacillus cereus</i>	Pos (8/8)	Pos (8/8)	Neg (0/8)	Neg (0/8)
<i>Pseudomonas fluorescens</i>	Neg (0/8)	Neg (0/8)	Pos (8/8)	Pos (8/8)
<i>Staphylococcus aureus</i>	Neg (0/8)	Neg (0/8)	Neg (0/8)	Neg (0/8)
<i>Listeria monocytogenes</i>	Neg (0/8)	Neg (0/8)	Neg (0/8)	Neg (0/8)
<i>Pseudomonas aeruginosa</i>	Neg (0/8)	Neg (0/8)	Neg (0/8)	Neg (0/8)
<i>Klebsiella pneumoniae</i>	Neg (0/8)	Neg (0/8)	Neg (0/8)	Neg (0/8)
<i>Escherichia coli</i>	Neg (0/8)	Neg (0/8)	Neg (0/8)	Neg (0/8)
<i>Staphylococcus epidermidis</i>	Neg (0/8)	Neg (0/8)	Neg (0/8)	Neg (0/8)
<i>Enterococcus faecium</i>	Neg (0/8)	Neg (0/8)	Neg (0/8)	Neg (0/8)
<i>Enterococcus faecalis</i>	Neg (0/8)	Neg (0/8)	Neg (0/8)	Neg (0/8)
<i>Enterobacter cloacae</i>	Neg (0/8)	Neg (0/8)	Neg (0/8)	Neg (0/8)
<i>Pseudomonas maltophilia</i>	Neg (0/8)	Neg (0/8)	Neg (0/8)	Neg (0/8)
<i>Proteus mirabilis</i>	Neg (0/8)	Neg (0/8)	Neg (0/8)	Neg (0/8)
<i>Candida albicans</i>	Neg (0/8)	Neg (0/8)	Neg (0/8)	Neg (0/8)
<i>Candida tropicalis</i>	Neg (0/8)	Neg (0/8)	Neg (0/8)	Neg (0/8)
<i>Candida parapsilosis</i>	Neg (0/8)	Neg (0/8)	Neg (0/8)	Neg (0/8)
<i>Candida glabrata</i>	Neg (0/8)	Neg (0/8)	Neg (0/8)	Neg (0/8)
<i>Candida krusei</i>	Neg (0/8)	Neg (0/8)	Neg (0/8)	Neg (0/8)

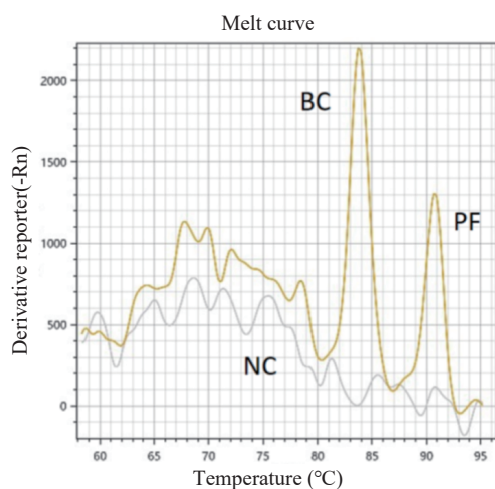


FIGURE 3. Dual EvaGreen-RAA assay using melting curves for mixed BC and PF in simulated milk samples with a concentration of 200 CFU/mL for each pathogen.

Abbreviation: RAA=recombinase aided amplification; NC=negative control; BC=*Bacillus cereus*; PF=*Pseudomonas fluorescens*.

dimers (10–12). In contrast to previously reported approaches, our study retained the T base at the 3' terminus of primers while selectively replacing only A, G, or C bases, thereby enhancing the stability of the 3'-end of the SAMRS primer.

Eva-green dye exhibits preferential binding to the minor groove region of all dsDNA double helices,

offering advantages of enhanced sensitivity and cost-effectiveness. However, its non-specific binding capacity to DNA double strands, including primer dimers, can potentially generate false positive results (13–14). The integration of SAMRS primers in our study effectively addressed this non-specificity issue. Both AGE and melting curve analyses confirmed that SAMRS primers successfully eliminated primer dimer formation.

The workflow of the EvaGreen-RAA assay, illustrated in Supplementary Figure S1 (available at <https://weekly.chinacdc.cn/>), demonstrates enhanced sensitivity and quantitative capability, as the amplicons generated by the reaction consist exclusively of target products, corroborating our most recent findings (15). Furthermore, the EvaGreen-RAA assay enables dual-target detection through HRM curve analysis by exploiting the differential T_m values of distinct amplification products. However, this study did not optimize primer concentration or the number of non-natural bases incorporated. An additional limitation concerns the persistent challenges in synthesizing non-natural bases. Despite these constraints, the EvaGreen-RAA assay provides a valuable platform for simple, rapid, and sensitive detection of pathogens of public health concern in primary laboratory settings.

The EvaGreen-RAA assay utilizing SAMRS primers

demonstrates superior sensitivity and specificity for detecting *B. cereus* and *P. fluorescens* in under 30 minutes, eliminating the need for complex RAA probe design. This approach provides a novel strategy for multiplexed pathogen detection in isothermal amplification systems.

Conflicts of interest: No conflicts of interest.

Acknowledgments: All the participants in this study.

Funding: Supported by Shandong Province Key Research and Development Plan (Major Scientific and Technological Innovation Project, 2023CXGC010711), the National Key R&D Program of China (2021YFC2301102), and the National Natural Science Foundation of China (82202593, U23A20106).

doi: 10.46234/ccdcw2025.079

* Corresponding authors: Xuejun Ma, maxj@ivdc.chinacdc.cn; Lingjun Li, lingjunlee@htu.edu.cn.

¹ National Key Laboratory of Intelligent Tracking and Forecasting for Infectious Diseases, NHC Key Laboratory of Medical Virology and Viral Diseases, National Institute for Viral Disease Control and Prevention, Chinese Center for Disease Control and Prevention, Beijing, China; ² State Key Laboratory of Antiviral Drugs, NMPA Key Laboratory for Research and Evaluation of Innovative Drug, Pingyuan Laboratory, School of Chemistry and Chemical Engineering, Henan Normal University, Xinxiang City, Henan Province, China.

Copyright © 2025 by Chinese Center for Disease Control and Prevention. All content is distributed under a Creative Commons Attribution Non Commercial License 4.0 (CC BY-NC).

Submitted: December 02, 2024

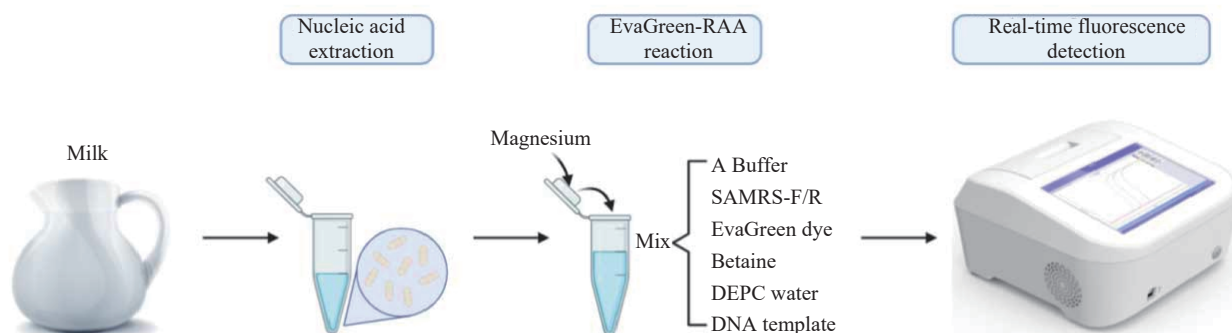
Accepted: March 30, 2025

Issued: April 04, 2025

REFERENCES

- Tayyarcan EK, Evran E, Guven K, Ekiz E, Acar Soykut E, Boyaci IH. Evaluating the efficacy of a phage cocktail against *Pseudomonas fluorescens* group strains in raw milk: microbiological, physical, and chemical analyses. *Arch Microbiol* 2024;206(6):283. <https://doi.org/10.1007/s00203-024-04008-1>.
- Meng L, Zhang RR, Dong L, Hu HY, Liu HM, Zheng N, et al. Characterization and spoilage potential of *Bacillus cereus* isolated from farm environment and raw milk. *Front Microbiol* 2022;13:940611. <https://doi.org/10.3389/fmicb.2022.940611>.
- Kowalska J, Maćkiw E, Korsak D, Postupolski J. Prevalence of *Bacillus cereus* in food products in Poland. *Ann Agric Environ Med* 2024;31(1): 8 – 12. <https://doi.org/10.26444/aaem/168580>.
- Amalfitano N, Patel N, Haddi ML, Benabid H, Pazzola M, Vacca GM, et al. Detailed mineral profile of milk, whey, and cheese from cows, buffaloes, goats, ewes, and dromedary camels, and efficiency of recovery of minerals in their cheese. *J Dairy Sci* 2024;107(11):8887 – 907. <https://doi.org/10.3168/jds.2023-24624>.
- Ma XJ. Isothermal amplification technology for diagnosis of COVID-19: current status and future prospects. *Zoonoses* 2022;2(1):5. <https://doi.org/10.15212/zoonoses-2021-0022>.
- Li FY, Guo YH, Sun ZL, Liu H, Zhao MC, Cui J, et al. Rapid two-stage amplification in a single tube for simultaneous detection of norovirus GII and group A rotavirus. *J Clin Lab Anal* 2023;37(5): e24858. <https://doi.org/10.1002/jcla.24858>.
- Nie MZ, Zhang RQ, Zhao MC, Tan H, Hu YX, Fan GH, et al. Development of a duplex recombinase-aided amplification assay for direct detection of *Mycoplasma pneumoniae* and *Chlamydia trachomatis* in clinical samples. *J Microbiol Methods* 2022;198:106504. <https://doi.org/10.1016/j.mimet.2022.106504>.
- Hoshika S, Chen F, Leal NA, Benner SA. Artificial genetic systems: self-avoiding DNA in PCR and multiplexed PCR. *Angew Chem Int Ed* 2010;49(32):5554 – 7. <https://doi.org/10.1002/anie.201001977>.
- Saladino R, Mincione E, Crestini C, Mezzetti M. Transformations of thiopyrimidine and thiopurine nucleosides following oxidation with dimethyldioxirane. *Tetrahedron* 1996;52(19):6759 – 80. [https://doi.org/10.1016/0040-4020\(96\)00289-x](https://doi.org/10.1016/0040-4020(96)00289-x).
- Sharma N, Hoshika S, Hutter D, Bradley KM, Benner SA. Recombinase-based isothermal amplification of nucleic acids with self-avoiding molecular recognition systems (SAMRS). *ChemBioChem* 2014;15(15):2268 – 74. <https://doi.org/10.1002/cbic.201402250>.
- Yang ZY, McLendon C, Hutter D, Bradley KM, Hoshika S, Frye CB, et al. Helicase-dependent isothermal amplification of DNA and RNA by using self-avoiding molecular recognition systems. *ChemBioChem* 2015;16(9):1365 – 70. <https://doi.org/10.1002/cbic.201500135>.
- Yang ZY, Le JT, Hutter D, Bradley KM, Overton BR, McLendon C, et al. Eliminating primer dimers and improving SNP detection using self-avoiding molecular recognition systems. *Biol Methods Protoc* 2020;5(1):bpaa004. <https://doi.org/10.1093/biomethods/bpaa004>.
- Zheng Y, Hu P, Ren HL, Wang H, Cao Q, Zhao Q, et al. RPA-SYBR Green I based instrument-free visual detection for pathogenic *Yersinia enterocolitica* in meat. *Anal Biochem* 2021;621:114157. <https://doi.org/10.1016/j.ab.2021.114157>.
- Tong SYC, Dakh F, Hurt AC, Deng YM, Freeman K, Fagan PK, et al. Rapid detection of the H275Y oseltamivir resistance mutation in influenza A/H1N1 2009 by single base pair RT-PCR and high-resolution melting. *PLoS One* 2011;6(6):e21446. <https://doi.org/10.1371/journal.pone.0021446>.
- Zhao ZJ, You YB, Hua SW, Shen XX, Li LJ, Ma XJ. Dye - based recombinase - aided amplification assay with enhanced sensitivity and specificity. *iLABMED* 2024;2(4):294 – 306. <https://doi.org/10.1002/ila2.51>.

SUPPLEMENTARY MATERIAL



SUPPLEMENTARY FIGURE S1. Workflow diagram of an EvaGreen-RAA assay.

Note: An EvaGreen-dye based recombinase aided amplification (EvaGreen-RAA) assay with SAMRS primers effectively avoids the production of primer dimers, thus improving the detection sensitivity while eliminating the addition of fluorescent probes for RAA. The EvaGreen-RAA assay provides a new approach for allowing the detection of multiple pathogens in the milk.

Abbreviation: SAMRS=self-avoiding molecular recognition system.

Notifiable Infectious Diseases Reports

Reported Cases and Deaths of National Notifiable Infectious Diseases — China, February 2025

Diseases	Cases	Deaths
Plague	0	0
Cholera	0	0
SARS-CoV	0	0
Acquired immune deficiency syndrome [†]	3,931	1,609
Hepatitis	142,691	116
Hepatitis A	2,222	0
Hepatitis B	120,756	35
Hepatitis C	15,806	78
Hepatitis D	19	0
Hepatitis E	3,199	3
Other hepatitis	689	0
Poliomyelitis	0	0
Human infection with H5N1 virus	0	0
Measles	309	0
Epidemic hemorrhagic fever	172	0
Rabies	4	7
Japanese encephalitis	0	0
Dengue	51	0
Anthrax	21	0
Dysentery	1,706	1
Tuberculosis	52,942	208
Typhoid fever and paratyphoid fever	215	0
Meningococcal meningitis	20	1
Pertussis	4,298	0
Diphtheria	0	0
Neonatal tetanus	1	0
Scarlet fever	2,551	0
Brucellosis	4,363	0
Gonorrhea	7,104	0
Syphilis	52,008	3
Leptospirosis	2	0
Schistosomiasis	2	0
Malaria	212	3
Human infection with H7N9 virus	0	0
COVID-19	22,966	1
Monkey pox [§]	56	0
Influenza	1,348,394	14

Continued

Diseases	Cases	Deaths
Mumps	3,833	0
Rubella	41	0
Acute hemorrhagic conjunctivitis	1,392	0
Leprosy	36	0
Typhus	37	0
Kala azar	39	0
Echinococcosis	423	0
Filariasis	0	0
Infectious diarrhea [¶]	242,791	1
Hand, foot and mouth disease	5,721	0
Total	1,898,332	1,964

* According to the National Bureau of Disease Control and Prevention.

† The number of deaths of acquired immune deficiency syndrome (AIDS) is the number of all-cause deaths reported in the month by cumulative reported AIDS patients.

§ Since September 20, 2023, Monkey pox was included in the management of Class B infectious diseases.

¶ Infectious diarrhea excludes cholera, dysentery, typhoid fever and paratyphoid fever.

The number of cases and cause-specific deaths refer to data recorded in National Notifiable Disease Reporting System in China, which includes both clinically-diagnosed cases and laboratory-confirmed cases. Only reported cases of the 31 provincial-level administrative divisions in the Chinese mainland are included in the table, whereas data of Hong Kong Special Administrative Region, Macau Special Administrative Region, and Taiwan, China are not included. Monthly statistics are calculated without annual verification, which were usually conducted in February of the next year for de-duplication and verification of reported cases in annual statistics. Therefore, 12-month cases could not be added together directly to calculate the cumulative cases because the individual information might be verified via National Notifiable Disease Reporting System according to information verification or field investigations by local CDCs.

doi: 10.46234/ccdcw2025.080

Copyright © 2025 by Chinese Center for Disease Control and Prevention. All content is distributed under a Creative Commons Attribution Non Commercial License 4.0 (CC BY-NC).

Submitted: March 26, 2025

Accepted: March 28, 2025

Issued: April 04, 2025

Youth Editorial Board

Director Lei Zhou

Vice Directors Jue Liu Tiantian Li Tianmu Chen

Members of Youth Editorial Board

Jingwen Ai	Li Bai	Yuhai Bi	Yunlong Cao
Gong Cheng	Liangliang Cui	Meng Gao	Jie Gong
Yuehua Hu	Jia Huang	Xiang Huo	Xiaolin Jiang
Yu Ju	Min Kang	Huihui Kong	Lingcai Kong
Shengjie Lai	Fangfang Li	Jingxin Li	Huigang Liang
Di Liu	Jun Liu	Li Liu	Yang Liu
Chao Ma	Yang Pan	Zhixing Peng	Menbao Qian
Tian Qin	Shuhui Song	Kun Su	Song Tang
Bin Wang	Jingyuan Wang	Linghang Wang	Qihui Wang
Xiaoli Wang	Xin Wang	Feixue Wei	Yongyue Wei
Zhiqiang Wu	Meng Xiao	Tian Xiao	Wuxiang Xie
Lei Xu	Lin Yang	Canqing Yu	Lin Zeng
Yi Zhang	Yang Zhao	Hong Zhou	

Indexed by Science Citation Index Expanded (SCIE), Social Sciences Citation Index (SSCI), PubMed Central (PMC), Scopus, Chinese Scientific and Technical Papers and Citations, and Chinese Science Citation Database (CSCD)

Copyright © 2025 by Chinese Center for Disease Control and Prevention

Under the terms of the Creative Commons Attribution-Non Commercial License 4.0 (CC BY-NC), it is permissible to download, share, remix, transform, and build upon the work provided it is properly cited. The work cannot be used commercially without permission from the journal.

References to non-China-CDC sites on the Internet are provided as a service to *CCDC Weekly* readers and do not constitute or imply endorsement of these organizations or their programs by China CDC or National Health Commission of the People's Republic of China. China CDC is not responsible for the content of non-China-CDC sites.

The inauguration of *China CDC Weekly* is in part supported by Project for Enhancing International Impact of China STM Journals Category D (PIIJ2-D-04-(2018)) of China Association for Science and Technology (CAST).



Vol. 7 No. 14 Apr. 4, 2025

Responsible Authority

National Disease Control and Prevention Administration

Sponsor

Chinese Center for Disease Control and Prevention

Editing and Publishing

China CDC Weekly Editorial Office
No.155 Changbai Road, Changping District, Beijing, China
Tel: 86-10-63150501, 63150701
Email: weekly@chinacdc.cn

CSSN

ISSN 2096-7071 (Print)

ISSN 2096-3101 (Online)

CN 10-1629/R1